Large-momentum-transfer elastic scattering of $\pi^{\pm}$, $K^{\pm}$, and $p^{\pm}$ on protons at 100 and 200 GeV/c

R. Rubinstein, W. F. Baker, D. P. Eartly, J. S. Klinger,* and A. J. Lennox
Fermi National Accelerator Laboratory, Batavia, Illinois 60510

R. M. Kalbach,† K. W. Krueger,‡ and A. E. Pifer
University of Arizona, Tucson, Arizona 85721

H. G. E. Kobrak and S. F. McHugh§
University of California at San Diego, LaJolla, California 92093

D. H. Kaplan,** P. Karchin,§ and J. Orear
Cornell University, Ithaca, New York 14853
(Received 29 May 1984)

Results are presented on $\pi^{\pm}p$, $K^{\pm}p$, and $p^{\pm}p$ elastic scattering measured with an apparatus having acceptance of $0.5<-t<2.5$ (GeV/c)^2 and $0.9<-t<11$ (GeV/c)^2 at 100 and 200 GeV/c, respectively. A diffractionlike dip is seen for the first time in the π^-p t distribution at $-t=4$ (GeV/c)^2. All meson-proton cross sections are found to be similar in the range $1<-t<2.5$ (GeV/c)^2, although some small systematic differences are observed. Cross sections for pp and $\bar{p}p$ are compared with previous data.

I. INTRODUCTION

This paper contains the final results of a Fermilab experiment which measured hadron-hadron elastic scattering at large momentum transfers; preliminary results have already been presented.[1–7] We shall be concerned with scattering at large $-t$ [defined here as $-t \gtrsim 1$ (see Ref. 8)], and incident momenta above ~ 50 GeV/c.

When this experiment was proposed, extensive data existed on pp elastic scattering (see, for example, Refs. 9–14) up to the highest CERN ISR momentum (equivalent to a laboratory momentum of 2100 GeV/c), and out to $-t$ of 14. Above ~ 150 GeV/c, a prominent diffractionlike dip in the t distribution at $-t=1.4$ appeared, but no other dips were observed. Data[15] on np scattering extended to $-t=4$, and showed very similar behavior to that of pp. For other reactions ($\pi^{\pm}p$, $K^{\pm}p$, $\bar{p}p$), data[10,16,17] at momenta above a few tens of GeV/c extended only to $-t\approx 2$, with no evidence of dips, although these were present in lower-momentum data.

Many models have been proposed which could fit the large $-t$ pp results, but probably because of the paucity of data, there was considerably less theoretical activity for πp. It was hoped that accurate πp large $-t$ data would help to differentiate between the various models.

This experiment was primarily designed to measure 200-GeV/c π^-p elastic scattering to $-t\sim 10$. Data were also obtained at ± 100 and ± 200 GeV/c for incident π, K, and p. One aim was to search for diffraction dips in πp elastic scattering; another was to study the near equality of $\pi^{\pm}p$ and $K^{\pm}p$ elastic scattering which had been observed at $-t\approx 1$, with no momentum dependence from 14 to 200 GeV/c.[10,18] A complementary experiment at CERN (Refs. 19–24) with incident momenta of 20, 30, and 50 GeV/c took data at about the same time as this experiment.

A. Models for high-momentum, large $-t$, elastic scattering

Over the past decade there have been many models proposed to explain features of high-momentum, large $-t$ elastic scattering. Some examples are given in the references of the preliminary publications on this experiment. In this section we will discuss only three models with which we shall later compare our data.

1. Chou-Yang Model (Ref. 25)

In this diffraction (or geometrical) model, the amplitude for the elastic scattering of particle A on particle B is related to a transform of the product of the form factors of A and B. The assumption is made that the electromagnetic form factors for A and B are the appropriate ones to use. This hypothesis can be tested in the pp case since considerable data on elastic scattering are available, and the electromagnetic form factors have been measured using electron-proton scattering. The agreement obtained between prediction and data is generally good, including prediction of the observed $-t\sim 1.4$ dip.[26] One problem, however, has been that the model predicts further dips at larger values of $-t$, which have not been observed experimentally.

A meson form factor can be derived using experimental meson-proton elastic-scattering data and the known proton form factor. This has been carried out[27] with πp data up to $-t=2$, and the results agree with the electromagnetic form factor as determined from pion electroproduction[28] and πe elastic scattering.[29] The kaon form factor

similarly obtained[27] is also in agreement with that obtained from Ke elastic scattering.[30] Alternatively, using an assumed meson form factor, the meson-proton t distribution can be predicted. An example of one such prediction for πp scattering, available before this experiment was carried out, is given in Ref. 31. It predicted a dip in the t distribution at $-t$ of ~ 5. Of course, other assumed pion form factors can give substantially different predictions for the t distribution.

Diffraction models in general predict $d\sigma/dt$ at fixed t should be independent of momentum, except for geometrical scaling effects (discussed later) due to the s dependence of the total cross section. Also the shape of $d\sigma/dt$ is usually suggestive of a diffraction pattern with a strong central maximum followed by secondary dips and maxima.

2. QCD

Lepage and Brodsky[32] have calculated large-angle hadron-hadron elastic scattering using lowest-order QCD where the quarks in both hadrons participate in a single collision. For large s and t they obtain

$$\frac{d\sigma}{dt} \propto s^{-10} F_{pp}(t/s) \quad \text{for } pp$$

and

$$\frac{d\sigma}{dt} \propto s^{-8} F_{\pi p}(t/s) \quad \text{for } \pi p \ .$$

Donnachie and Landshoff[33] have made a similar calculation in which the quarks in hadron 1 scatter independently off the quarks in hadron 2 with the result

$$\frac{d\sigma}{dt} \propto s^{-8} f_{pp}(t/s) \quad \text{for } pp$$

and

$$\frac{d\sigma}{dt} \propto s^{-7} f_{\pi p}(t/s) \quad \text{for } \pi p \ .$$

They furthermore obtain a power-law dependence for $d\sigma/dt$ in the region $-t \ll s$:

$$\left.\begin{aligned} &\frac{d\sigma}{dt} \propto |t|^{-8} \quad \text{for } pp \\ &\qquad \text{and} \\ &\frac{d\sigma}{dt} \propto |t|^{-7} \quad \text{for } \pi p \end{aligned}\right\} \text{ independent of } s \ .$$

It has been pointed out[34] that if QCD radiative corrections are added, the Lepage-Brodsky result stays about the same, but the Donnachie-Landshoff result then approaches that of Lepage-Brodksy.

3. Geometrical scaling (Refs. 35–37)

In this approach, the elastic-scattering amplitude as a function of energy s and impact parameter b, $T(s,b)$, is given by $T(b/R(s))$; all of the energy dependence in the cross section is contained in the radial scale parameter $R(s)$. This leads to the following expressions for the total and elastic differential cross sections:

$$\sigma_T \propto R^2 \ , \quad d\sigma/dt \propto R^4 f(R^2 t) \ ,$$

where f is some universal function. Using the above two expressions, it is readily seen that a graph of $d\sigma/dt$ normalized to the optical point, plotted against $t\sigma_T$, should be a universal curve.

In the simplest form of geometrical scaling, the universal curve would be the same for all incident particles. However, it was soon determined[38,39] that this was too simple, and the functions depended on the incident-particle type.

B. Data existing prior to this experiment

1. pp

A large amount of data on pp elastic scattering existed prior to this experiment. For example, at 31 GeV/c, data extend to $-t$ of 24;[40] at 400 GeV/c to $-t$ of 14 (Ref. 13); and at $\sqrt{s}$ of 53 GeV to $-t$ of 10.[14] Figure 1 shows some pp data[12–14,41,42] out to $-t=6$. The dominant feature is the emergence, above ~ 150 GeV/c, of a diffractionlike dip at $-t=1.4$, followed by a second maximum. There are now considerable data on the momentum dependence of the dip depth and position. No other dips are observed; the t distributions are smooth and monotonic in other regions of t. For $-t \geq 3$, the fall with increasing $-t$ is considerably slower than at small $-t$.

Comparisons of large $-t$ data with the QCD predictions discussed above have been made,[32,33,43,44] and reasonable agreement is observed.

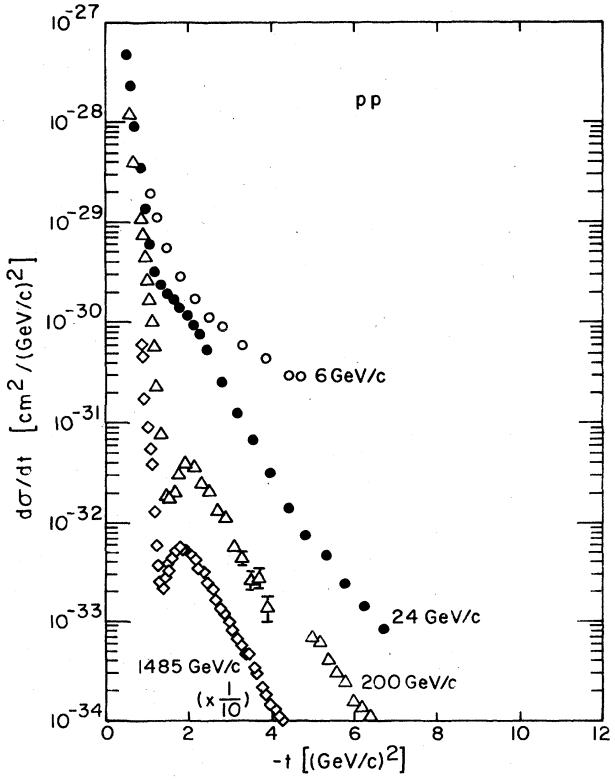

FIG. 1. Proton-proton elastic-scattering data (Refs. 12–14, 41, and 42).

2. *np*

Data[15] on this reaction up to 360 GeV/c existed out to $-t$ of 4. The observed t distributions are similar to those for pp.

3. $\bar{p}p$

Very little data above 50 GeV/c were available above $-t$ of 1; at low momenta ($\sim$10 GeV/c), $\bar{p}p$ distributions[45–48] have considerable structure, but within the limited data that were available in the momentum range considered here, these structures had died out.

4. $\pi^{\pm}p$

Prior to this experiment (and the complementary CERN experiment), data at $\sim$20 GeV/c extended to $-t=6$.[49] Several experiments[10,16,17,50] above 20 GeV/c have provided data to $-t\approx 2$. The data above 50 GeV/c showed little charge or momentum dependence, and no structures like the pp dip at $-t=1.4$ were observed. Unlike the pp case, low-energy ($\sim$10 GeV/c) (Refs. 45 and 51) πp scattering has dips, which die out as momentum is increased; the change in slope at $-t=3$ of the 22-GeV/c $\pi^- p$ data[49] shown in Fig. 2 is the remnant of such a $-t\approx 2.8$ dip.

5. $K^{\pm}p$

The limited data available[10,18,50,52–54] showed little charge or momentum dependence above $\sim$14 GeV/c, with cross sections similar to those of πp (see Fig. 3, taken from Ref. 18).

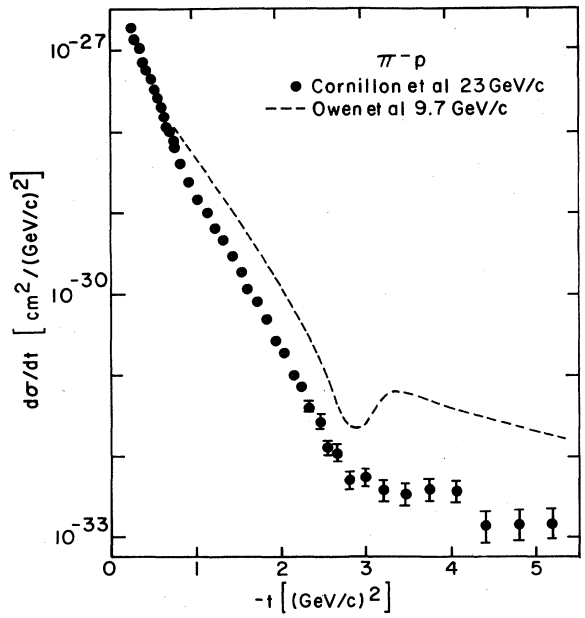

FIG. 2. $\pi^- p$ elastic scattering at 22.6 GeV/c (Ref. 49) and a curve through the 9.7-GeV/c data of Ref. 45.

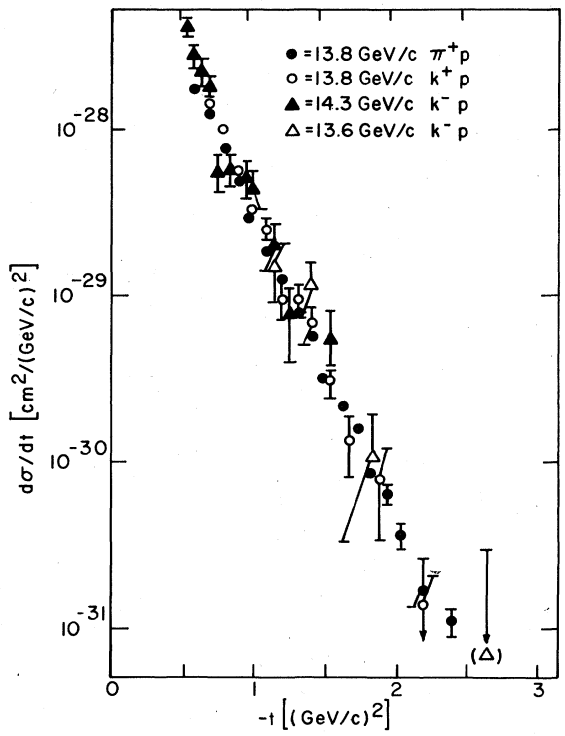

FIG. 3. πp and Kp elastic scattering near 14 GeV/c (figure from Ref. 18).

II. EXPERIMENTAL METHOD

A. Introduction

The design of the experiment was driven by the desire to measure small cross sections, of order 10^{-36} cm^2/(GeV/c)^2. This necessitated high incident-beam rates, large geometrical acceptance, and a liquid-hydrogen target whose length was a significant fraction of an interaction length. Because inelastic background was expected to be much greater than the elastic signal, good momentum and angle measurements were required on both outgoing particles. To save running time, elastic scattering of more than one incident-particle type should be measured simultaneously using gas Cherenkov counters for particle identification.

The experimental arrangement used is shown in Fig. 4. Hadrons (π,K,p) in a beam of known momentum and direction were elastically scattered off the protons in a 1-m liquid-hydrogen target. The scattering angles and momenta of the two outgoing particles were measured in separate magnetic spectrometers, each consisting of analysis magnets with proportional wire chambers (PWC's) on both sides to determine particle trajectories; triggering was by means of predetermined combinations of counters in four scintillation-counter hodoscopes (two in each spectrometer), which provided fast although imprecise momentum and angle measurements for each particle.

The experiment was designed specifically to measure 200-GeV/c $\pi^- p$ elastic scattering out to $-t$ of over 10. Early in the data-taking, 50-GeV/c CERN results[19] became available showing the existence of a dip in the $\bar{p}p$ t distribution at $-t=1.4$, and verification of this effect at

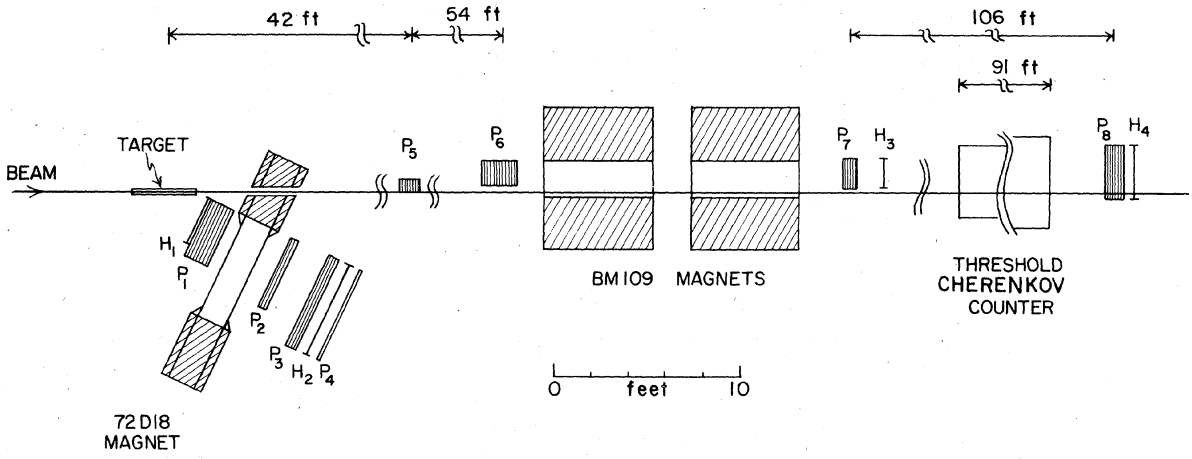

FIG. 4. Experimental layout. H_1—H_4 are scintillation-counter hodoscopes; P_1—P_8 are proportional-wire-chamber arrays. Not shown are veto counters around the liquid-hydrogen target, helium bags in the forward spectrometer, monitor telescopes, and apparatus in the incident beam such as scintillation counters, proportional wire chambers, segmented wire ionization chambers, and a differential Cherenkov counter.

100 GeV/c became an important goal. Some data were also taken at 100 and 200 GeV/c with positive incident particles. No equipment was moved when the beam momentum was changed. Currents in the BM109 analysis magnets of the forward spectrometer were reduced by a factor of two between 200 and 100 GeV/c, with their polarity following the beam polarity. The $-t$ acceptance of the apparatus covered the ranges approximately $0.9 < -t < 11$ at 200 GeV and $0.5 < -t < 2.5$ at 100 GeV/c. In the following sections, we describe more fully various parts of the experimental equipment. Additional details are given in Refs. 4—7.

B. Beam

The experiment used the M6E beam in the Meson Area at Fermilab. Figure 5 shows the schematic beam optics and the beam layout; a more complete description is available in Refs. 55 and 56. The time structure of the beam was that of the accelerator rf, with particles arriving in "buckets" of about 1-nsec length separated by 18.8 nsec. Beam particles were recorded by two scintillation counters (B_1 and B_2 in Fig. 4) together with a halo veto (A) that had a hole for the beam to pass through. A 32-element scintillator hodoscope at a momentum-dispersed intermediate focus was used to measure the relative momentum of each incident particle to an accuracy of ~0.04%. This hodoscope, together with another 16-element hodoscope upstream of the hydrogen target, was also used to determine if there were two or more beam particles in one bucket.

A differential gas Cherenkov counter[57] (DISC), located in a highly parallel section of the beam, tagged incident particles of a given mass in order to measure cross sections for more than one particle type simultaneously (see Sec. III H).

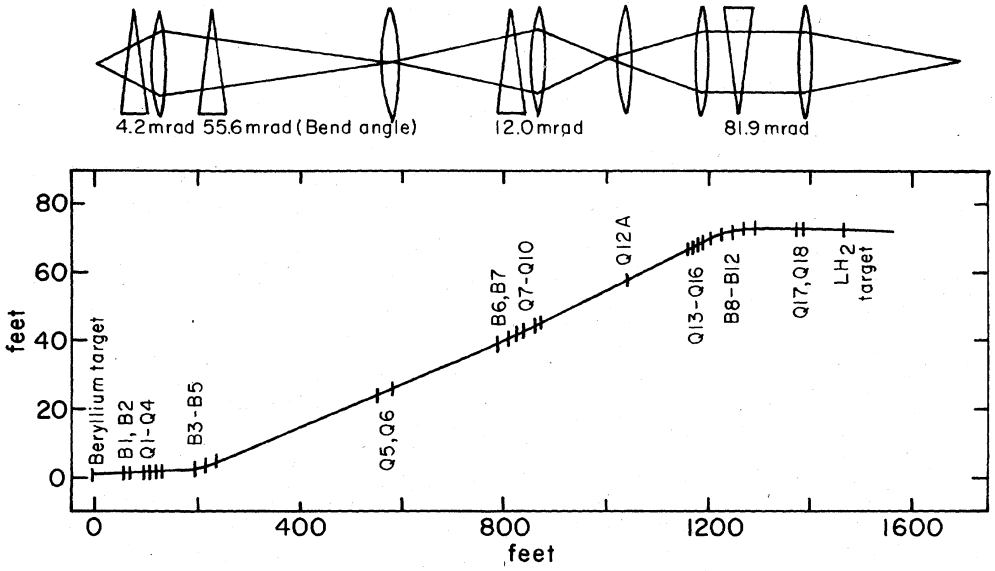

FIG. 5. Schematic beam optics and beam layout. Q is a quadrupole magnet; B is a dipole bending magnet.

The beam was made close to parallel through the experiment (less than 0.3-mrad divergence) so that determination of individual beam particle directions was unnecessary. Typical intensities during the run were up to $\sim 10^7$ particles/sec.

C. Hydrogen target

The target was a cylindrical vessel, 1 m along the beam direction and 7.6 cm in diameter, constructed of 0.25 mm Mylar. It was filled with hydrogen liquefied by a small helium refrigerator. During empty-target runs, the hydrogen was transferred to a reservoir above the target. Three sides of the target were covered by veto counters to improve rejection of inelastic collisions. A three-counter telescope ("N monitor") viewing the target at $\sim 30°$ was used as a monitor of the incident beam flux.

D. Forward spectrometer

Trajectory and momentum information on the forward scattered particle was obtained from four sets of PWC's (P_5, P_6, P_7, and P_8 in Fig. 4) located on either side of two BM109 analysis magnets; each BM109 had an aperture 72 in. along the beam line $\times 24$ in. wide $\times 8$ in. high. The total field integral was 2600 kG in. at 200 GeV/c and half of that at 100 GeV/c. The magnet horizontal aperture and placement gave the upper limit to the $-t$ acceptance of the experiment of ~ 11 (GeV/c)^2 at 200 GeV/c and ~ 2.6 (GeV/c)^2 at 100 GeV/c. Each set of PWC's contained at least two x (horizontal coordinate) chambers and at least one y chamber. All of the PWC's were sufficiently large that they accepted any elastic event that gave a trigger. Two hodoscopes H_3 and H_4 were used in the trigger; H_3 consisted of seven counters 2.75 in. wide $\times 7.5$ in. high place side by side, and H_4 consisted of seven partially overlapping counters each 9.4 in wide $\times 14.5$ in. high. To form the event trigger, twofold coincidences were made between each H_3 counter and its corresponding H_4 counter; the trigger was vetoed if there was a signal from more than one H_3 element or more than two H_4 elements. The counter placement was determined by Monte Carlo simulation of the experiment.

Helium bags were used in the upstream part of the spectrometer to reduce air scattering. Downstream of the analysis magnets was a large threshold gas Cherenkov counter filled with helium at pressures below one atmosphere. Particles traversing this counter had to pass through the 1-in.-thick mirror glass, so the counter was placed close to the final PWC's to minimize errors caused by multiple scattering and interactions in the glass.

E. Recoil spectrometer

The spectrometer for the recoil proton was based on a 72D18 magnet, with aperture 18 in. along the particle direction $\times 72$ in. wide $\times 18$ in. high; its field integral was 350 kG in. for both 100- and 200-GeV/c data-taking. In order to maximize the acceptance for elastic scattering, the magnet was placed at 65° to the incident beam and close to the hydrogen target; a hole in the magnet return iron yoke allowed the beam and forward scattered particles to pass through.

Particle momenta and trajectories were determined by several sets of PWC's, as seen in Fig. 4. P_1 upstream of the magnet, and sets P_2 and P_3 downstream, each contained two x measurements; P_1 contained three y measurements and P_4 had one y measurement. Because of the large horizontal sizes needed, the P_3 and P_4 chambers were composed of two adjacent PWC's. All PWC sets were large enough to record every elastic event giving a trigger.

Two hodoscopes (H_1 and H_2) located on either side of the magnet were used in the trigger. H_1 contained six elements each ~ 6 in. $\times 6$ in.; H_2 was composed of six elements 12 in. horizontal $\times 24$ in. vertical, with each element consisting of two counters. A coincidence matrix formed between the H_1 and H_2 hodoscopes favored elastic events from the hydrogen target and was used in making the trigger decision. The matrices used for each incident momentum were determined by Monte Carlo simulation of the experiment. The trigger was vetoed if there was a signal from more than one counter in either hodoscope.

F. Cherenkov counters

1. Beam differential counter

This counter was located in a parallel section of the incident beam; similar counters (called DISC counters) are described in Ref. 57. Cherenkov light produced at an angle of 25 mrad in the 5-m-long helium gas radiator was

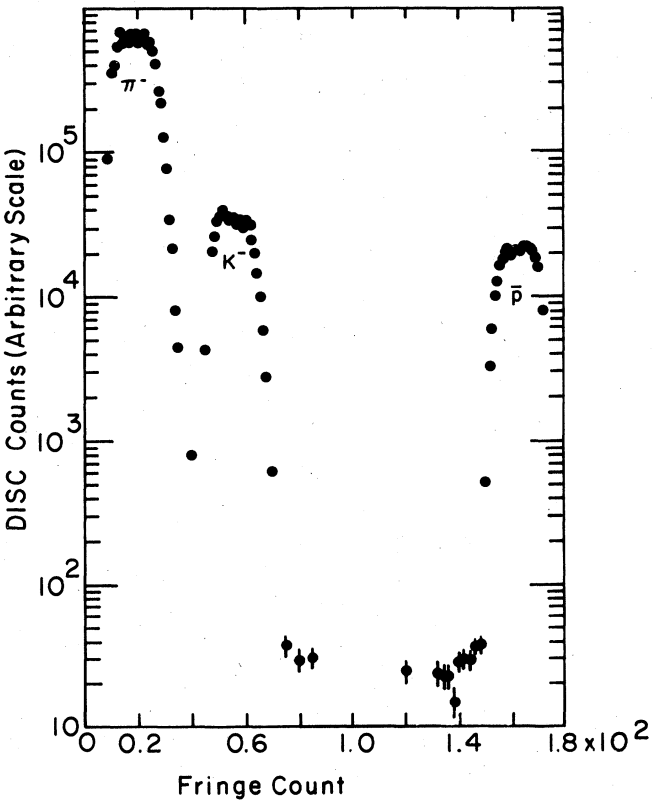

FIG. 6. DISC pressure curve at 100 GeV/c (negative incident particles).

TABLE I. Typical beam composition.

Momentum	Polarity	π	K	p
100 GeV/c	+	0.63	0.05	0.32
100 GeV/c	−	0.92	0.05	0.03
200 GeV/c	+	0.17	0.03	0.80
200 GeV/c	−	0.95	0.05	0.008

reflected through a chromatic correction system and an adjustable diaphragm onto eight RCA 31000M photomultipliers arranged in a circle. Six coincident photomultiplier signals were required. Relative values of the helium gas pressure and refractive index were obtained by electronically counting fringes of a laser refractometer mounted onto the gas vessel. Typical gas pressures were about 9 atm. An example of a DISC pressure curve is given in Fig. 6. From such curves, beam compositions were obtained (Table I), and also the absolute beam momenta were determined to an accuracy of about ±0.5%. The counter efficiency depended on beam conditions and on the diaphragm opening, which was varied to achieve adequate rejection of unwanted particles. The efficiencies obtained ranged from 9% for 200-GeV/c K^- to 82% for 100-GeV/c protons. The presence or absence of the counter output was recorded for every trigger.

2. *Threshold Cherenkov counter*

This counter was 28 m long, 1.5 m in diameter, with four adjacent spherical mirrors focusing light onto a single RCA 31000M photomultiplier; this counter, with a shorter 9-m-long radiator, had been built for a previous elastic-scattering experiment.[58] The helium gas pressure was set above the kaon threshold but below the proton threshold, so that protons gave no signal; noninteracting beam particles passed through an optically deadened region of the counter. For each elastic event, the photomultiplier output was recorded using an analog-to-digital converter (ADC), and also a latch bit was set if the pulse was above a fixed (low) threshold. At 100 GeV/c, pions and kaons could be separated by the counter, as illustrated in Figs. 7(a), 7(b), and 7(c), where we give ADC outputs for −100-GeV/c elastic events; Fig. 7(a) is for all events, while Figs. 7(b) and 7(c) are for those events where the beam Cherenkov counter indicated kaons and pions, respectively. The zero or very small (pedestal) signals are due to antiprotons. Some contamination remains because there are cases where a beam pion and kaon were in the same beam-timing rf "bucket." The beam Cherenkov counter could indicate the kaon while the pion could elastically scatter and give a signal in the threshold counter. The effect could be reduced if events were used only where the beam hodoscopes indicated only one incident particle in the bucket. Contaminations in the various particle signals were extensively studied in this manner.

At 200-GeV/c, the helium gas pressure in the counter was set at 4.5 psia (just below the proton threshold), while at 100 GeV/c it was either 7.1 or 8.5 psia. The number of photomultiplier photoelectrons for pions was generally between 10 and 20.

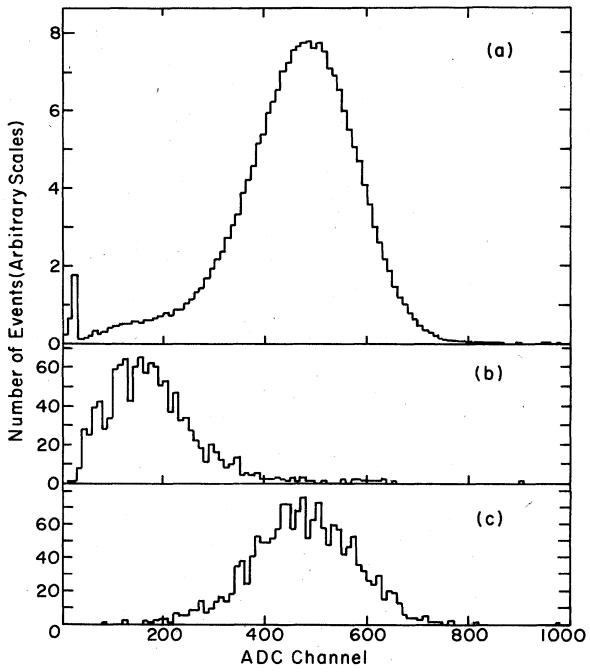

FIG. 7. Pulse-height spectra from the threshold Cherenkov counter at −100 GeV/c, as measured using the ADC. (a) All elastic events. (b) Elastic events where the beam Cherenkov counter indicated a kaon. (c) Elastic events where the Cherenkov counter indicated a pion.

G. Fast logic

The fast-logic system identified events where the trajectories and momenta of both outgoing particles from the hydrogen target were consistent with those expected for an elastic event. A beam particle was identified by the coincidence $B_1 \cdot B_2 \cdot \bar{A}$; the counters around the hydrogen target discussed earlier were then added in veto, followed by coincidences with the H_1 hodoscope elements. The H_1H_2 recoil-arm matrix was then formed, and its output was used as a pretrigger to temporarily disable the experiment; it initiated storage of most of the PWC and counter information until signals from the forward counters were received and a recoil-forward matrix could be formed. If this matrix (determined by Monte Carlo simulation of the experiment) was satisfied, the event data were transferred to the PDP11/45 on-line computer and then onto magnetic tape. All of the matrices in the fast logic were made using commercial fan-ins, fan-outs, and coincidence circuits.

TABLE II. Typical counting rates at 200 GeV/c for negative incident particles (rates given per 1-sec accelerator spill).

Beam particles	10^7
Beam + veto counters + hodoscope H_1	4×10^5
Beam + veto counters + recoil-arm matrix	9×10^3
Trigger rate	40
Elastic events (after analysis)	2

Typical counting rates in the experiment are given in Table II. At 200 GeV/c, about 4% of the triggers were found to be elastic events; at 100 GeV/c this increased to 47%, since the acceptance extended to lower $-t$ values and consequently larger elastic cross sections.

H. Proportional wire chambers

The experiment used 31 PWC's with a total of 7800 wires. Some of the PWC's were those used in an earlier elastic scattering experiment.[58] They had 2-mm wire spacing (in some chambers, adjacent wires were ganged together to give an effective 4-mm spacing). The readout system was based on the Nevis Laboratory design of Sippach,[59] using long stripline delay cables between the chambers and the experiment counting room. Other PWC's were of Cornell University type,[13,60] and used a readout system employing shift registers mounted on the chambers.[61] These chambers had wire spacings of either 16 or 20 wires to the inch. Typical PWC efficiencies measured during the run were above 90%.

III. DATA ANALYSIS

A. Introduction

The analysis of the data which had been written onto magnetic tape was carried out on the Fermilab CYBER 175 computers. Tracks were first determined from the PWC hits, and then event selection was made by applying elastic kinematic constraints to the scattering angles and momenta of the outgoing particles; Cherenkov-counter data were examined to determine the incident-particle type. Several other calculations, such as acceptance and corrections to the final cross sections, were also carried out.

B. Reconstruction

The reconstruction programs first found the eight track segments from the PWC data: x and y projections, both before and after the spectrometer magnets in each arm. Least-squares fits to all possible PWC hit clusters were used, although the PWC's generally had only one hit each per elastic event. The tracks obtained were limited to those which extrapolated to hodoscope elements giving the trigger. Tracks upstream of the spectrometer magnets had to extrapolate to a common point in the hydrogen target volume. Other requirements imposed at this stage of the analysis were that the track segments in each arm had to intersect close to the magnet centers, and that the momentum of the forward track be within 10% of the incident beam momentum. Generally there were only one or two tracks per segment which fitted all of the above criteria.

In the recoil arm, there were only two x PWC's upstream of the magnet. If there was a hit in only one of these chambers, this was still sufficient to determine the recoil proton momentum when it was taken together with a track segment downstream of the magnet.

C. Event selection

The vector momentum of each particle leaving the hydrogen target was obtained as described above. The momentum of each incident beam particle was derived from the known mean momentum together with information from the momentum hodoscope (see Sec. II B); its direction was taken to be the mean beam direction, since the angular spread of the beam was small. The kinematics of elastic scattering at 100 and 200 GeV/c in the t range measured here are almost independent of the incident-particle type (π,K,p), and no particle selection was done at this stage.

Four quantities were calculated from the momenta and angles of the outgoing particles:

(i) $\delta p_f = p_f(\text{measured}) - p_f(\theta_f(\text{measured}))$,

where p_f is the forward momentum, θ_f (measured) is the measured forward scattering angle, and $p_f(\theta_f(\text{measured}))$ is the expected forward momentum calculated for an elastic scattering with scattering angle θ_f (measured);

(ii) $\delta p_r = p_r(\text{measured}) - p_r(\theta_f(\text{measured}))$,

where p_r is the recoil momentum;

(iii) $\delta\theta_r = \theta_r(\text{measured}) - \theta_r(\theta_f(\text{measured}))$,

where θ_r is the recoil scattering angle; and

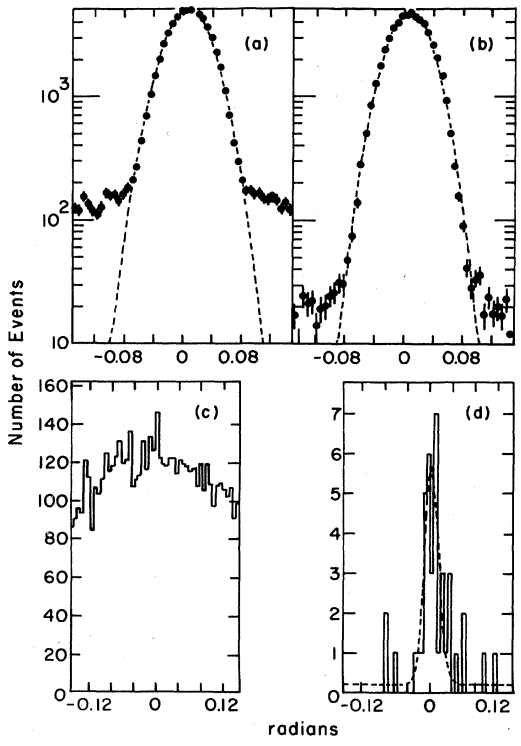

FIG. 8. Coplanarity distributions for 200-GeV/c negative-incident-particle data. (a) Events in the range $1.0 < -t < 1.5$. (b) As (a), after cuts on the other variables. (c) Events for $-t > 3.5$. (d) As (c), after cuts on the other variables; a maximum-likelihood fit to the signal plus background is also shown.

(iv) $\delta\phi$=coplanarity=$\phi_f+\phi_r$,

where ϕ_f and ϕ_r are the forward and recoil azimuthal angles.

Each of the four quantites δp_f, $\delta\theta_f$, $\delta\theta_r$, and $\delta\phi$ should be zero for an elastic event. Due to measurement errors, uncertainty in the knowledge of incident beam properties, etc., they each have a distribution around a mean of zero. The widths of the four distributions were determined from the experimental data, and cuts (which were t-dependent) at three standard deviations were applied to each quantity. Figure 8 shows coplanarity distributions before and after the cuts had been applied to the other variables.

After all of the cuts had been carried out, histograms were made of the number of events as a function of t, with t being determined from the angle of the recoil proton.

D. Acceptance

The acceptance of the apparatus for elastic events was determined by a Monte Carlo calculation. Some of the inputs to the calculation were the measured incident-beam properties, the hydrogen-target length, the location and sizes of the hodoscope elements, magnet apertures, PWC's, and the trigger-coincidence matrices. The acceptances at 100 and 200 GeV/c are shown in Fig. 9.

The shape of the acceptance close to its upper and lower t limits were very sensitive to uncertainties in beam momenta and directions; because of this, we have only derived cross sections in the ranges $0.5 \leq -t \leq 2.5$ at 100 GeV/c, and $0.9 \leq -t \leq 11.0$ at 200 GeV/c.

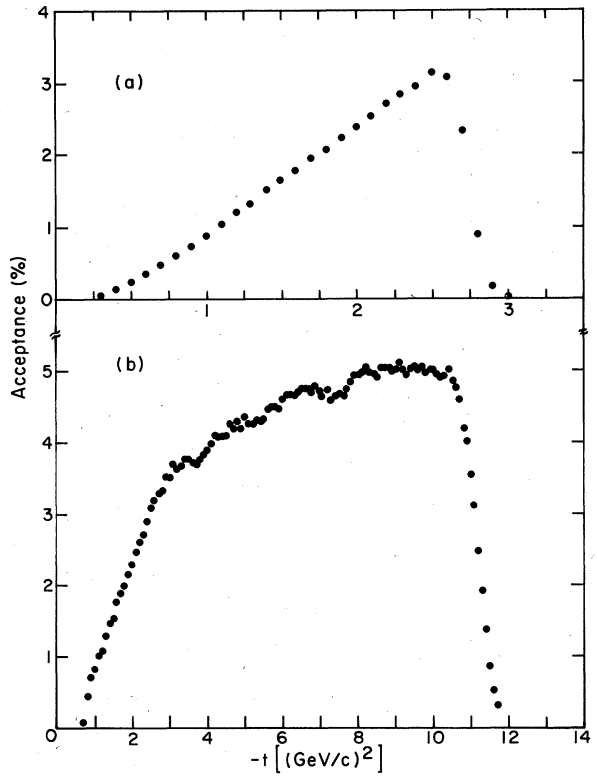

FIG. 9. Geometrical acceptance of the apparatus. (a) 100 GeV/c. (b) 200 GeV/c.

E. Analysis-program efficiency

The Monte Carlo calculation described above was also used to determine the efficiency with which the reconstruction and event selection programs found elastic events. Elastic events generated by the Monte Carlo calculation were converted to PWC and hodoscope hits, including experimentally observed resolutions and measured PWC efficiencies; random PWC background hits, obtained from actual data, were added. These events were passed through the analysis programs, and the analysis efficiencies derived. They were typically ~90%, with no measurable t dependence.

F. Inelastic background

Background still remaining under the signal, after all of the event selection cuts, was subtracted using the coplanarity distributions as illustrated in Fig. 8. A fit was made to the distribution for each t bin using a Gaussian-shaped signal and a broad Gaussian shaped background; the fitted background under the signal was then subtracted. At small $-t$, these backgrounds were typically 1% or 2%, rising to a maximum of 30% at $-t=3$, and then falling to 10% at $-t=10$.

The above corrections were determined for pions, which constituted the bulk of our data. For other particles, where it was difficult to accurately determine the correction because of the small numbers of events, the same fractional correction as for pions was applied.

G. Intensity effects

As noted earlier, the beam intensity was monitored by the scintillation counters B_1 and B_2 in the incident beam as well as the N telescope viewing the hydrogen target. It was found that the ratio of elastic events to beam flux was a function of beam intensity. This effect was caused by two factors. Large B_1 and B_2 photomultiplier pulses due to more than one particle in an rf bucket could cause a discriminator dead time extending over the succeeding rf bucket. If two beam particles came in the same bucket, one could scatter elastically while the other could scatter inelastically and set a veto counter or multiplicity veto.

Because of fluctuations in the primary-proton-beam intensity, there was a wide range of secondary intensities present during data taking. The ratio of the number of elastic events to N counts (occurring during the equipment live time) was plotted against the N counts per accelerator beam spill, as illustrated in Fig. 10. A linear extrapolation was made to obtain the value at zero intensity. In a similar manner, the calibration of the N monitor in terms of the number of incident beam particles was obtained by extrapolation to zero intensity.

For minority particles, adequate statistics were not available to carry out the above extrapolation procedure. However, the corrections should be independent of particle type, and so the slope of the minority-particle extrapo-

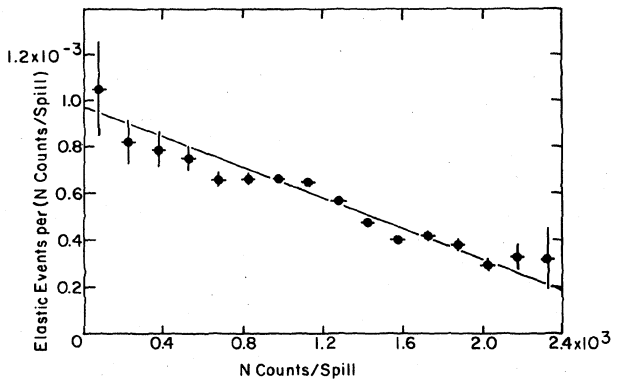

FIG. 10. Rates of elastic events to N monitor counts as a function of N monitor counts per accelerator beam spill (200-GeV/c negative-incident-particle data).

lation to zero intensity was taken to be the same as for pions.

H. Particle identification

Incident-particle identification for events identified as elastic used the two Cherenkov counters C_B and C_F. C_B was set on various incident particles during the data taking, most commonly $\bar{p}$ during negative beam running, and K^+ during positive beam running; the C_F gas pressure was set at almost all times between the kaon and proton thresholds. Extensive studies were carried out on the C_F ADC distributions for different incident particles tagged by C_B. Thus, we could derive appropriate ADC cuts for each particle type, and determine the contamination from the other particle types.

1. Pions

C_B was not used in the determination of pion cross sections. At 100 GeV/c, the C_F ADC signal alone was used to separate pions from kaons and protons, with a negligible ($<1\%$) contamination of the signal. At 200 GeV/c, protons were eliminated using C_F, but it was not possible to separate pions from kaons with an ADC cut. The pion data were corrected for the kaons remaining in the signal by assuming that the K and π elastic cross sections are equal (a good approximation as we shall see later) and using the measured K/π ratios in the incident beam (see Table I).

2. Kaons

At 100 GeV/c, as noted above, C_F alone was used to obtain a clean kaon signal. Thus, kaon data were obtained with C_B set on any incident particle, although only relative cross sections were obtained in this way. Absolute cross sections were obtained, as described in Sec. III G above, only from the data taken with C_B set on kaons.

At 200 GeV/c, only data with C_B set on kaons were used; however, a correction was still required since a kaon and another particle could be in the same rf bucket. Using information from the beam hodoscope counters, it was determined that pion contamination in the kaon signal was 25% for negative incident particles and under 2% for positive incident particles; corrections were made to the results for this.

3. Antiprotons and protons

The antiproton data used in obtaining cross sections at both 100 and 200 GeV/c were taken with C_B set on antiprotons, together with a cut on C_F pulse height. (An exception was a small amount of 100 GeV/c running, where C_F only was used to separate antiprotons from other particles; these data were not used in the determination of absolute cross sections.) For protons, use of C_F alone reduced contamination to negligible levels, although only runs with C_B set on protons were used to obtain the absolute normalization.

I. Corrections

Several small corrections, not previously discussed, had to be made to the elastic cross sections we derived, and they are noted here.

(i) After the C_F ADC cuts discussed in Sec. III H were made, there was still some remaining contamination by unwanted particles and some remaining loss of wanted particles. (Up to 4% for $p,\bar{p}$; 14% for 200-GeV/c π^+; for K see above.)

(ii) Interactions of incoming or outgoing particles in the hydrogen target (8—18%).

(iii) Decay of particles through the apparatus (pions, 1%; kaons, 5% at 200 GeV/c and 10% at 100 GeV/c).

(iv) Radiative corrections, obtained using the methods of Refs. 62 and 63. These depended on the incident-particle type, the incident momentum, and t; they varied from $<1\%$ for 100-GeV/c protons at $-t<5$ to 9.7% for 200-GeV/c π^- at $-t=10.25$.

(v) Empty-target effects; interactions of outgoing particles in the spectrometers; δ rays from the target causing vetoes (total 3%).

Except for (iv), the above corrections affect only the normalization of the data, and not the shape of the t distributions.

J. Overall uncertainties in absolute cross sections

The preceding sections have discussed the corrections to the data and the method of obtaining absolute cross sections. There are uncertainties in some of these procedures which give rise to uncertainties in absolute cross-section values but do not affect the shape of the t distributions obtained. Our estimates of the systematic uncertainties in the overall normalization of the data are given in Table III.

TABLE III. Systematic uncertainties in overall normalization.

	100 GeV/c	200 GeV/c
π^+	±15%	±15%
π^-	±15%	±15%
K^+	±15%	±20%
K^-	±15%	±30%
p	±15%	±15%
$\bar{p}$	±15%	±35%

TABLE IV. 100 GeV/c results for positive incident particles. Statistical errors only are listed. The additional overall normalization uncertainties are given in Table III. The bin center is at $-t$; total width of the bin is Δt. Units for $d\sigma/dt$ are cm^2/(GeV/c)^2. For those bins in which no signal above background was observed, the cross sections are given as upper limits representing one event.

$-t$ [(GeV/c)^2]	Δt [(GeV/c)^2]	$d\sigma/dt$ π^+	$d\sigma/dt$ K^+	$d\sigma/dt$ p
0.55	0.10	$(4.44\pm0.05)\times10^{-28}$	$(4.14\pm0.23)\times10^{-28}$	$(3.72\pm0.06)\times10^{-28}$
0.65	0.10	$(2.09\pm0.03)\times10^{-28}$	$(1.80\pm0.12)\times10^{-28}$	$(1.29\pm0.03)\times10^{-28}$
0.75	0.10	$(1.13\pm0.02)\times10^{-28}$	$(1.01\pm0.08)\times10^{-28}$	$(5.14\pm0.15)\times10^{-29}$
0.85	0.10	$(6.16\pm0.12)\times10^{-29}$	$(6.44\pm0.54)\times10^{-29}$	$(2.23\pm0.09)\times10^{-29}$
0.95	0.10	$(3.32\pm0.08)\times10^{-29}$	$(3.46\pm0.36)\times10^{-29}$	$(7.94\pm0.46)\times10^{-30}$
1.05	0.10	$(1.84\pm0.06)\times10^{-29}$	$(1.96\pm0.24)\times10^{-29}$	$(2.90\pm0.27)\times10^{-30}$
1.15	0.10	$(1.14\pm0.04)\times10^{-29}$	$(1.40\pm0.19)\times10^{-29}$	$(1.16\pm0.15)\times10^{-30}$
1.25	0.10	$(7.06\pm0.30)\times10^{-30}$	$(7.02\pm1.22)\times10^{-30}$	$(4.94\pm0.92)\times10^{-31}$
1.35	0.10	$(3.52\pm0.20)\times10^{-30}$	$(4.70\pm0.98)\times10^{-30}$	$(1.90\pm0.56)\times10^{-31}$
1.45	0.10	$(2.19\pm0.15)\times10^{-30}$	$(4.14\pm0.87)\times10^{-30}$	$(5.4\ \pm2.8)\times10^{-32}$
1.55	0.10	$(1.46\pm0.12)\times10^{-30}$	$(1.80\pm0.54)\times10^{-30}$	$(6.4\ \pm2.9)\times10^{-32}$
1.65	0.10	$(1.04\pm0.10)\times10^{-30}$	$(7.6\ \pm3.4)\times10^{-31}$	$(8.4\ \pm3.2)\times10^{-32}$
1.75	0.10	$(5.72\pm0.69)\times10^{-31}$	$(5.5\ \pm2.9)\times10^{-31}$	$(7.9\ \pm3.0)\times10^{-32}$
1.85	0.10	$(3.85\pm0.54)\times10^{-31}$	$(6.5\ \pm3.0)\times10^{-31}$	$(1.17\pm0.35)\times10^{-31}$
1.95	0.10	$(1.58\pm0.34)\times10^{-31}$	$(6.1\ \pm2.8)\times10^{-31}$	$(4.0\ \pm1.9)\times10^{-32}$
2.05	0.10	$(2.04\pm0.37)\times10^{-31}$		$(5.7\ \pm2.3)\times10^{-32}$
2.15	0.10	$(9.0\ \pm2.4)\times10^{-32}$		$(4.5\ \pm2.0)\times10^{-32}$
2.15	0.30		$(1.1\ \pm0.6)\times10^{-31}$	
2.25	0.10	$(5.4\ \pm1.8)\times10^{-32}$		$(3.4\ \pm1.6)\times10^{-32}$
2.35	0.10	$(3.9\ \pm1.5)\times10^{-32}$		$(3.1\ \pm1.5)\times10^{-32}$
2.45	0.10	$(2.2\ \pm1.1)\times10^{-32}$		
2.45	0.30		$<3.0\times10^{-32}$	
2.50	0.20			$(1.2\ \pm0.7)\times10^{-32}$

TABLE V. 100 GeV/c results for negative incident particles. See caption of Table IV.

$-t$ [(GeV/c)^2]	Δt [(GeV/c)^2]	$d\sigma/dt$ π^-	$d\sigma/dt$ K^-	$d\sigma/dt$ $\bar{p}$
0.55	0.10	$(4.34\pm0.01)\times10^{-28}$	$(3.97\pm0.08)\times10^{-28}$	$(2.55\pm0.06)\times10^{-28}$
0.65	0.10	$(2.08\pm0.01)\times10^{-28}$	$(1.87\pm0.05)\times10^{-28}$	$(9.33\pm0.29)\times10^{-29}$
0.75	0.10	$(1.12\pm0.01)\times10^{-28}$	$(1.08\pm0.03)\times10^{-28}$	$(3.46\pm0.15)\times10^{-29}$
0.85	0.10	$(6.16\pm0.03)\times10^{-29}$	$(5.78\pm0.19)\times10^{-29}$	$(1.69\pm0.10)\times10^{-29}$
0.95	0.10	$(3.47\pm0.02)\times10^{-29}$	$(3.54\pm0.13)\times10^{-29}$	$(6.54\pm0.53)\times10^{-30}$
1.05	0.10	$(1.94\pm0.01)\times10^{-29}$	$(2.25\pm0.10)\times10^{-29}$	$(2.40\pm0.29)\times10^{-30}$
1.15	0.10	$(1.11\pm0.01)\times10^{-29}$	$(1.27\pm0.07)\times10^{-29}$	$(6.81\pm1.43)\times10^{-31}$
1.25	0.10	$(6.44\pm0.07)\times10^{-30}$	$(7.10\pm0.47)\times10^{-30}$	$(1.35\pm0.60)\times10^{-31}$
1.35	0.10	$(3.71\pm0.05)\times10^{-30}$	$(4.16\pm0.34)\times10^{-30}$	$(5.0\ \pm3.5)\times10^{-32}$
1.45	0.10	$(2.19\pm0.04)\times10^{-30}$	$(2.83\pm0.27)\times10^{-30}$	
1.50	0.20			$(1.1\ \pm1.1)\times10^{-32}$
1.55	0.10	$(1.40\pm0.03)\times10^{-30}$	$(1.17\pm0.17)\times10^{-30}$	
1.65	0.10	$(8.53\pm0.20)\times10^{-31}$	$(1.45\pm0.18)\times10^{-30}$	
1.70	0.20			$(2.8\ \pm1.6)\times10^{-32}$
1.75	0.10	$(5.41\pm0.16)\times10^{-31}$	$(7.04\pm1.14)\times10^{-31}$	
1.85	0.10	$(3.30\pm0.12)\times10^{-31}$	$(4.25\pm0.86)\times10^{-31}$	
1.90	0.20			$(3.2\ \pm1.6)\times10^{-32}$
1.95	0.10	$(2.10\pm0.09)\times10^{-31}$	$(2.62\pm0.65)\times10^{-31}$	
2.05	0.10	$(1.33\pm0.07)\times10^{-31}$	$(1.39\pm0.46)\times10^{-31}$	
2.10	0.20			$(3.5\ \pm1.6)\times10^{-32}$
2.15	0.10	$(8.30\pm0.53)\times10^{-32}$	$(1.88\pm0.52)\times10^{-31}$	
2.25	0.10	$(4.83\pm0.39)\times10^{-32}$	$(9.5\ \pm3.5)\times10^{-32}$	
2.30	0.20			$(3.1\ \pm1.4)\times10^{-32}$
2.35	0.10	$(3.05\pm0.30)\times10^{-32}$	$(9.1\ \pm3.3)\times10^{-32}$	
2.45	0.10	$(1.72\pm0.22)\times10^{-32}$	$(3.8\ \pm2.2)\times10^{-32}$	$(1.2\ \pm1.2)\times10^{-32}$

IV. RESULTS

A. Introduction

The results of this experiment are presented in tabular form in Tables IV–VII, and graphically in Figs. 11–20. Errors quoted are statistical and represent one standard deviation; for those bins in which no signal above background was observed, the cross sections are given as upper limits representing one event. The systematic errors on the results have been discussed in Sec. III J.

B. General features of the results

All 12 sets of differential cross sections measured here are in agreement with the corresponding lower $-t$ data,[10,16,17] within the quoted statistical and systematic errors, in the t ranges of overlap. Our data, together with the lower $-t$ data, show a steep fall of many decades from the optical point as $-t$ increases from zero.

1. pp

We can compare our pp data with previously available results[10,12,13] over the entire t range of our measurements. As can be seen in Figs. 11 and 12, there is good agreement at both 100 and 200 GeV/c, giving additional confidence in our normalization procedure. We see the well-known $-t=1.4$ dip at 200 GeV/c, while at 100 GeV/c our data are also consistent with a small dip at the same t value.

TABLE VI. 200 GeV/c results for positive incident particles. See caption of Table IV.

$-t$ [(GeV/c)^2]	Δt [(GeV/c)^2]	$d\sigma/dt$ π^+	$d\sigma/dt$ K^+	$d\sigma/dt$ p
0.95	0.10	$(2.21\pm0.07)\times10^{-29}$	$(2.80\pm0.49)\times10^{-29}$	$(6.68\pm0.17)\times10^{-30}$
1.05	0.10	$(1.32\pm0.05)\times10^{-29}$	$(2.57\pm0.44)\times10^{-29}$	$(2.88\pm0.11)\times10^{-30}$
1.15	0.10	$(7.75\pm0.31)\times10^{-30}$	$(1.12\pm0.26)\times10^{-29}$	$(9.79\pm0.48)\times10^{-31}$
1.25	0.10	$(4.21\pm0.22)\times10^{-30}$	$(4.7\ \pm1.6)\times10^{-30}$	$(3.21\pm0.28)\times10^{-31}$
1.35	0.10	$(2.42\pm0.15)\times10^{-30}$	$(3.2\ \pm1.3)\times10^{-30}$	$(9.79\pm1.44)\times10^{-32}$
1.45	0.10	$(1.62\pm0.12)\times10^{-30}$	$(3.4\ \pm1.2)\times10^{-30}$	$(3.55\pm0.83)\times10^{-32}$
1.55	0.10	$(1.02\pm0.09)\times10^{-30}$	$(1.2\ \pm0.7)\times10^{-30}$	$(3.09\pm0.75)\times10^{-32}$
1.65	0.10	$(5.58\pm0.66)\times10^{-31}$	$(1.0\ \pm0.6)\times10^{-30}$	$(2.00\pm0.57)\times10^{-32}$
1.75	0.10	$(3.78\pm0.52)\times10^{-31}$	$(1.3\ \pm0.6)\times10^{-30}$	$(2.82\pm0.67)\times10^{-32}$
1.85	0.10	$(1.66\pm0.33)\times10^{-31}$	$(9.0\ \pm5.2)\times10^{-31}$	$(4.93\pm0.83)\times10^{-32}$
1.95	0.10	$(1.61\pm0.32)\times10^{-31}$		$(3.87\pm0.73)\times10^{-32}$
2.05	0.10	$(1.05\pm0.25)\times10^{-31}$		$(4.88\pm0.78)\times10^{-32}$
2.05	0.30		$(1.8\ \pm1.3)\times10^{-31}$	
2.15	0.10	$(3.8\ \pm1.5)\times10^{-32}$		$(4.20\pm0.71)\times10^{-32}$
2.25	0.10	$(3.6\ \pm1.4)\times10^{-32}$		$(1.93\pm0.46)\times10^{-32}$
2.35	0.10	$(1.9\ \pm1.0)\times10^{-32}$		$(2.54\pm0.51)\times10^{-32}$
2.35	0.30		$(2.2\ \pm1.3)\times10^{-31}$	
2.45	0.10	$(9.1\ \pm6.5)\times10^{-33}$		$(2.85\pm0.55)\times10^{-32}$
2.55	0.10	$(1.7\ \pm0.9)\times10^{-32}$		$(1.71\pm0.41)\times10^{-32}$
2.65	0.10			$(1.51\pm0.37)\times10^{-32}$
2.65	0.30		$(<6.9)\times10^{-32}$	
2.75	0.10			$(1.65\pm0.38)\times10^{-32}$
2.75	0.30	$(2.6\ \pm1.9)\times10^{-33}$		
2.85	0.10			$(1.46\pm0.35)\times10^{-32}$
2.95	0.10			$(8.1\ \pm2.5)\times10^{-33}$
3.05	0.10			$(6.5\ \pm2.2)\times10^{-33}$
3.05	0.30	$(2.2\ \pm1.6)\times10^{-33}$		
3.15	0.10			$(3.3\ \pm1.5)\times10^{-33}$
3.25	0.10			$(7.3\ \pm2.1)\times10^{-33}$
3.35	0.10			$(3.6\ \pm1.5)\times10^{-33}$
3.35	0.30	$(9.6\ \pm9.6)\times10^{-34}$		
3.45	0.10			$(4.2\ \pm1.6)\times10^{-33}$
3.55	0.10			$(4.9\ \pm1.9)\times10^{-33}$
3.65	0.10			$(3.8\ \pm1.7)\times10^{-33}$
3.65	0.30	$(<1.1)\times10^{-33}$		
3.75	0.10			$(2.2\ \pm1.3)\times10^{-33}$
4.00	0.40			$(7.3\ \pm3.6)\times10^{-34}$
4.55	0.70			$(3.9\ \pm2.0)\times10^{-34}$
5.45	1.10			$(1.7\ \pm1.0)\times10^{-34}$
6.55	1.10			$(5.4\ \pm5.4)\times10^{-35}$
8.15	2.10			$(2.6\ \pm2.6)\times10^{-35}$
10.25	2.10			$(<2.8)\times10^{-35}$

TABLE VII. 200 GeV/c results for negative incident particles. See caption of Table IV.

$-t$ [(GeV/c)^2]	Δt [(GeV/c)^2]	$d\sigma/dt$ π^-	$d\sigma/dt$ K^-	$d\sigma/dt$ $\bar{p}$
0.95	0.10	$(2.83\pm0.02)\times10^{-29}$	$(3.47\pm0.68)\times10^{-29}$	$(6.6\ \pm1.7)\times10^{-30}$
1.05	0.10	$(1.72\pm0.01)\times10^{-29}$	$(2.65\pm0.56)\times10^{-29}$	$(2.6\ \pm1.0)\times10^{-30}$
1.15	0.10	$(1.00\pm0.01)\times10^{-29}$	$(2.28\pm0.45)\times10^{-29}$	$(9.2\ \pm5.3)\times10^{-31}$
1.25	0.10	$(5.60\pm0.06)\times10^{-30}$	$(5.0\ \pm2.0)\times10^{-30}$	
1.35	0.10	$(3.26\pm0.04)\times10^{-30}$		
1.40	0.20		$(3.2\ \pm1.2)\times10^{-30}$	
1.45	0.10	$(1.93\pm0.03)\times10^{-30}$		
1.45	0.50			$<4.5\times10^{-32}$
1.55	0.10	$(1.21\pm0.02)\times10^{-30}$		
1.60	0.20		$(2.1\ \pm0.8)\times10^{-30}$	
1.65	0.10	$(7.28\pm0.18)\times10^{-31}$		
1.75	0.10	$(4.89\pm0.14)\times10^{-31}$		
1.85	0.10	$(3.16\pm0.11)\times10^{-31}$		
1.85	0.30		$(4.9\ \pm2.8)\times10^{-31}$	
1.95	0.10	$(1.94\pm0.08)\times10^{-31}$		
1.95	0.50			$(6.2\ \pm4.4)\times10^{-32}$
2.05	0.10	$(1.15\pm0.06)\times10^{-31}$		
2.15	0.10	$(8.89\pm0.52)\times10^{-32}$		
2.15	0.30		$(3.8\ \pm2.2)\times10^{-31}$	
2.25	0.10	$(4.87\pm0.37)\times10^{-32}$		
2.35	0.10	$(2.87\pm0.28)\times10^{-32}$		
2.45	0.10	$(1.80\pm0.21)\times10^{-32}$		
2.45	0.30		$<1.3\times10^{-31}$	
2.45	0.50			$(4.4\ \pm3.2)\times10^{-32}$
2.55	0.10	$(1.16\pm0.17)\times10^{-32}$		
2.65	0.10	$(9.9\ \pm1.5)\times10^{-33}$		
2.75	0.10	$(3.8\ \pm0.9)\times10^{-33}$		
2.85	0.10	$(3.4\ \pm0.8)\times10^{-33}$		
2.95	0.10	$(1.4\ \pm0.5)\times10^{-33}$		
3.05	0.10	$(9.2\ \pm3.8)\times10^{-34}$		
3.05	0.70			$(2.1\ \pm1.5)\times10^{-32}$
3.30	0.40	$(3.6\ \pm1.1)\times10^{-34}$		
3.70	0.40	$(1.3\ \pm0.8)\times10^{-34}$		
3.75	0.70			$(1.9\ \pm1.3)\times10^{-32}$
4.10	0.40	$<4.3\times10^{-35}$		
4.45	0.70			$<9.8\times10^{-33}$
4.50	0.40	$(8.2\ \pm5.8)\times10^{-35}$		
4.90	0.40	$(2.0\ \pm0.9)\times10^{-34}$		
5.30	0.40	$(2.6\ \pm1.0)\times10^{-34}$		
6.00	1.00	$(4.3\ \pm2.5)\times10^{-35}$		
7.00	1.00	$(5.4\ \pm2.7)\times10^{-35}$		
8.00	1.00	$(1.3\ \pm1.3)\times10^{-35}$		
9.00	1.00	$<1.3\times10^{-35}$		
10.25	1.50	$(3.1\ \pm1.8)\times10^{-35}$		

2. $\bar{p}p$

Our 100-GeV/c data (Fig. 13) confirm the existence of the $-t=1.4$ dip in this reaction which had previously been observed[19] only at 50 GeV/c. The 200-GeV/c results (Fig. 14) have less statistical accuracy, but are consistent with the same effect.

3. π^-p

The dominant feature of the 200-GeV/c t distribution shown in Fig. 15 is the prominent dip at $-t=4$; it is followed by a second maximum and then a slow decrease with increasing $-t$. This effect had not previously been observed. (Dips have been observed in low-momentum πp scattering, as noted earlier, but they die out as momentum is increased, and disappear by $\sim$20 GeV/c.) Also, the slope of the t distribution in the range $1<-t<3.5$ is not constant, but has considerable variation with t.

4. *Other meson-proton scattering*

All of the other meson-proton t distributions measured here (Figs. 16–20) show no dips or breaks over the limited t range studied.

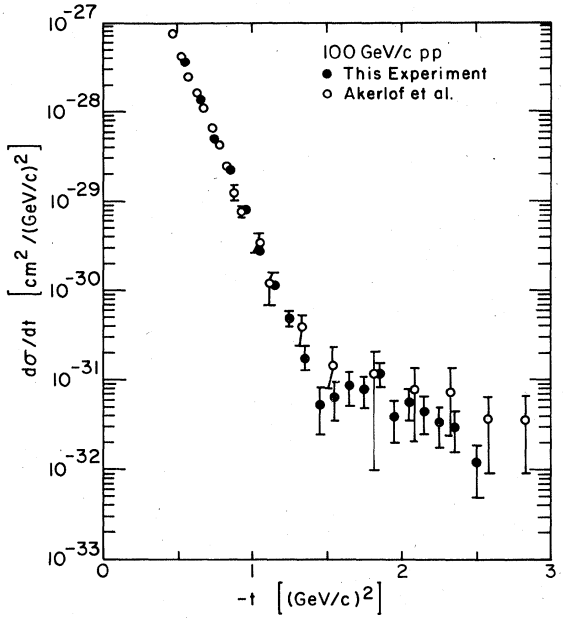

FIG. 11. Proton-proton elastic scattering at 100 GeV/c; data from this experiment and Ref. 10 (not all points plotted, for clarity).

C. Discussion

1. pp

Our data for $-t<4$, together with those from several other experiments,[14,22,42] are shown in Fig. 21. The development of the $-t=1.4$ dip with momentum above ~ 100 GeV/c is clearly seen, as is the movement of the dip position. Parametrizations of the data of Fig. 21, and some comparison with models, have been made in Ref. 22, where preliminary values of our results were included.

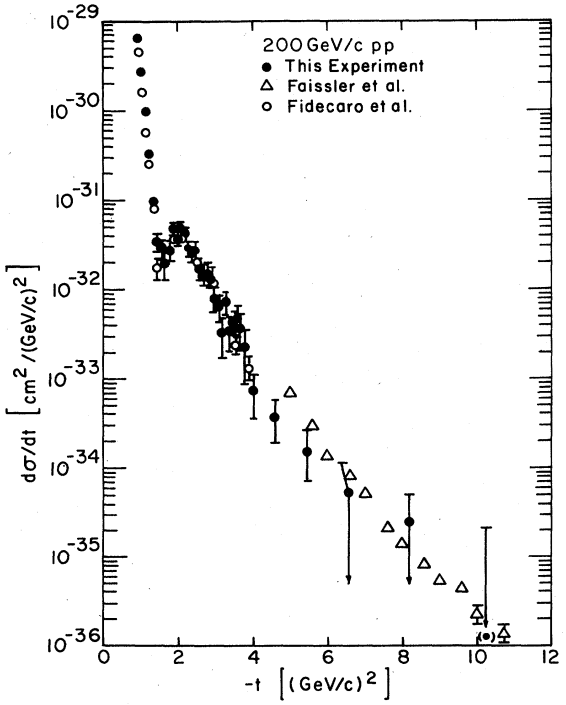

FIG. 12. Proton-proton elastic scattering at 200 GeV/c; data from this experiment and Refs. 12 and 13 (not all points plotted, for clarity).

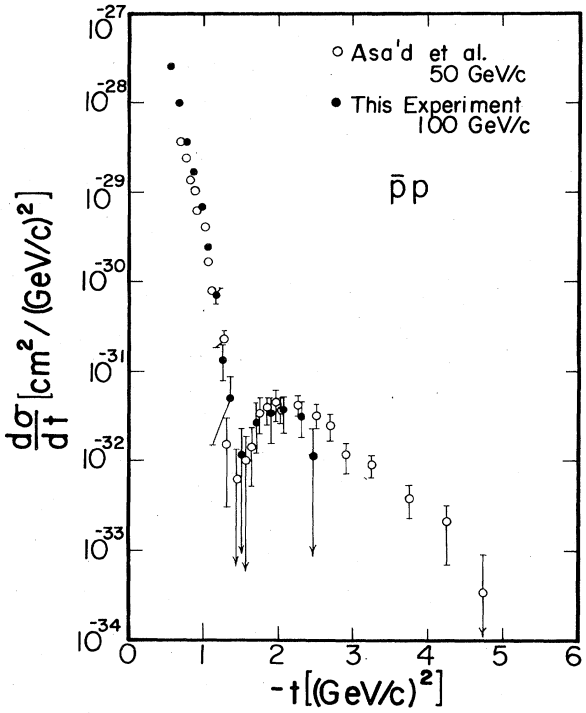

FIG. 13. Antiproton-proton elastic scattering at 100 GeV/c from this experiment, together with 50 GeV/c data from Ref. 19.

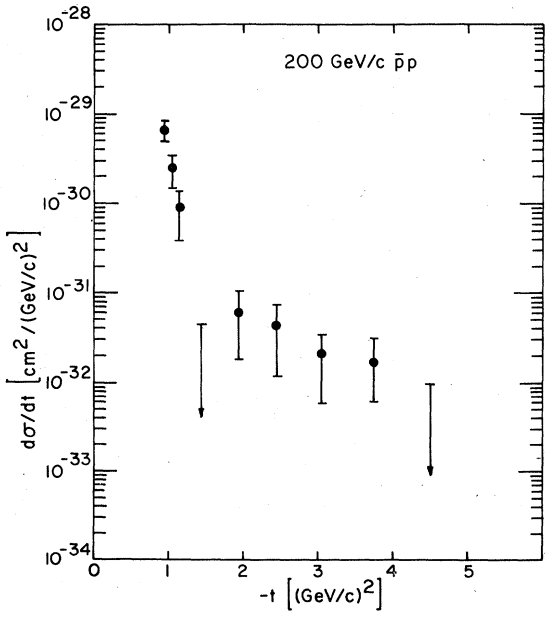

FIG. 14. Antiproton-proton elastic scattering at 200 GeV/c.

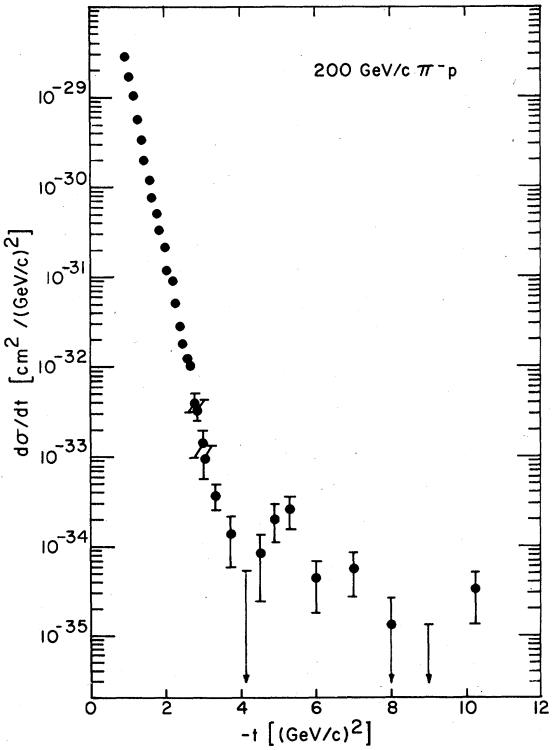

FIG. 15. $\pi^- p$ elastic scattering at 200 GeV/c.

2. $\bar{p}p$

Within the experimental errors, no dependence of the cross section with momentum is observed between 50 and 200 GeV/c (Fig. 22). In that momentum range we see no movement of the $-t \approx 1.4$ dip with momentum, a subject of some recent theoretical interest.[64,65] Expected movements, however, are smaller than could be seen with the available statistics. At $\sqrt{s} = 540$ GeV,[66] the dip has become just a kink, which has moved to $-t \approx 0.8$; this inward $-t$ movement as σ_T increases is consistent with geometrical scaling. However, at 30 GeV/c,[23] the dip has moved out to $-t = 1.7$, inconsistent with geometrical scaling, and other explanations are required.[67,68]

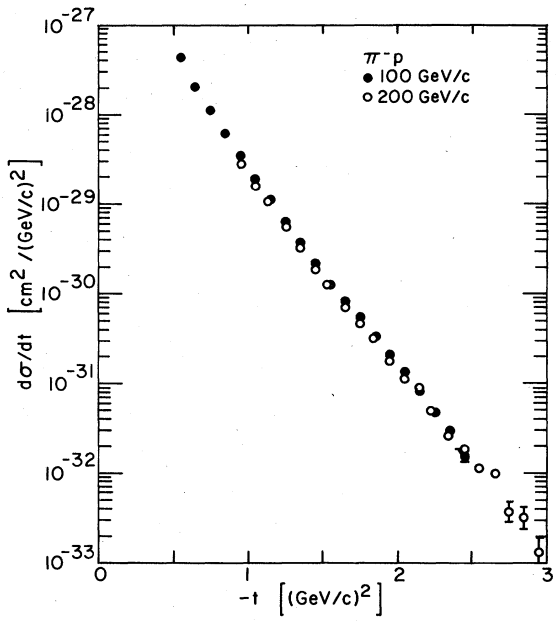

FIG. 17. $\pi^- p$ elastic scattering at 100 and 200 GeV/C.

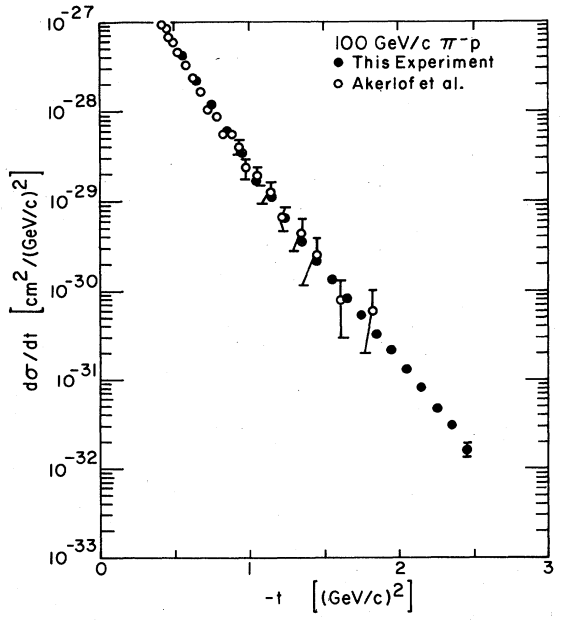

FIG. 16. $\pi^- p$ elastic scattering at 100 GeV/c; data from this experiment and Ref. 10 (not all points plotted, for clarity).

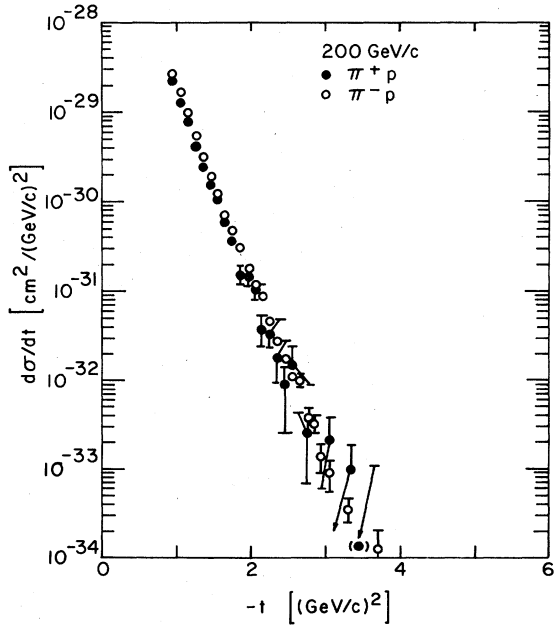

FIG. 18. $\pi^{\pm} p$ elastic scattering at 200 GeV/c.

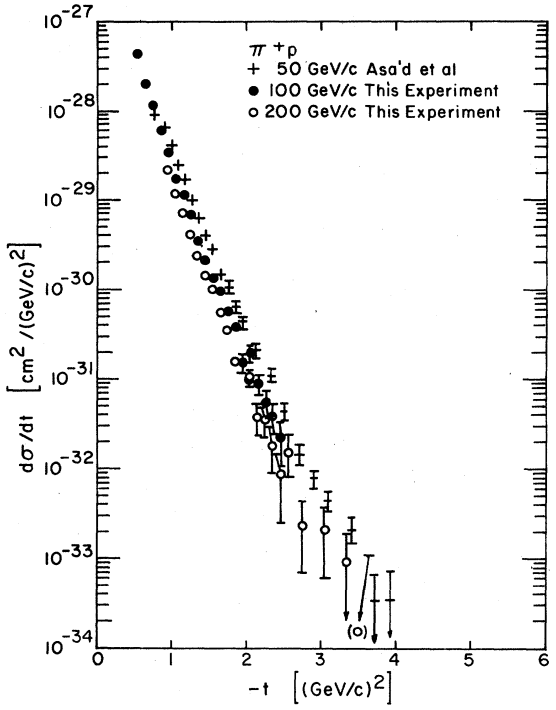

FIG. 19. π^+p elastic scattering at 100 and 200 GeV/c (this experiment), and 50 GeV/c (Ref. 20).

In Fig. 23, we show the incident momentum dependence of $d\sigma/dt$ at several fixed values of t interpolated from this experiment and Refs. 19, 23, and 45. The cross section at a fixed value of t falls with increasing momentum, but the rate of fall decreases and the cross sections then become independent of momentum. This behavior is qualitatively similar to that for pp, discussed in Ref. 22.

Figure 24 gives a comparison of pp and $\bar{p}p$ data, and within the errors we see little difference between the two reactions at these momenta except in the immediate dip region.

3. 200-GeV/c π^-p

The data (Fig. 15) show a drop of ~ 6 decades from $-t=1$ to a minimum at $-t=4$, followed by a second maximum and then a slow fall with increasing $-t$. When our data are taken together with those of Ref. 10, the shape of $d\sigma/dt$ out to $-t$ of 4 is considerably more complex than a simple exponential form Ae^{Bt}. Local values of B decrease from 10 to 6.5 to 4.5 (GeV/c)$^{-2}$ at $-t$ of 0, 0.6, and 2.0, respectively. At $-t\sim 3$, B increases to 5.5 (GeV/c)$^{-2}$ as the dip is approached—a similar phenomenon to the increase in pp values of B as the $-t=1.4$ dip is approached.

Results for 50-GeV/c π^-p (Ref. 20) (shown in Fig. 25 together with our 200 GeV/c data) do not show the $-t=4$ dip (although there is a change of slope at the

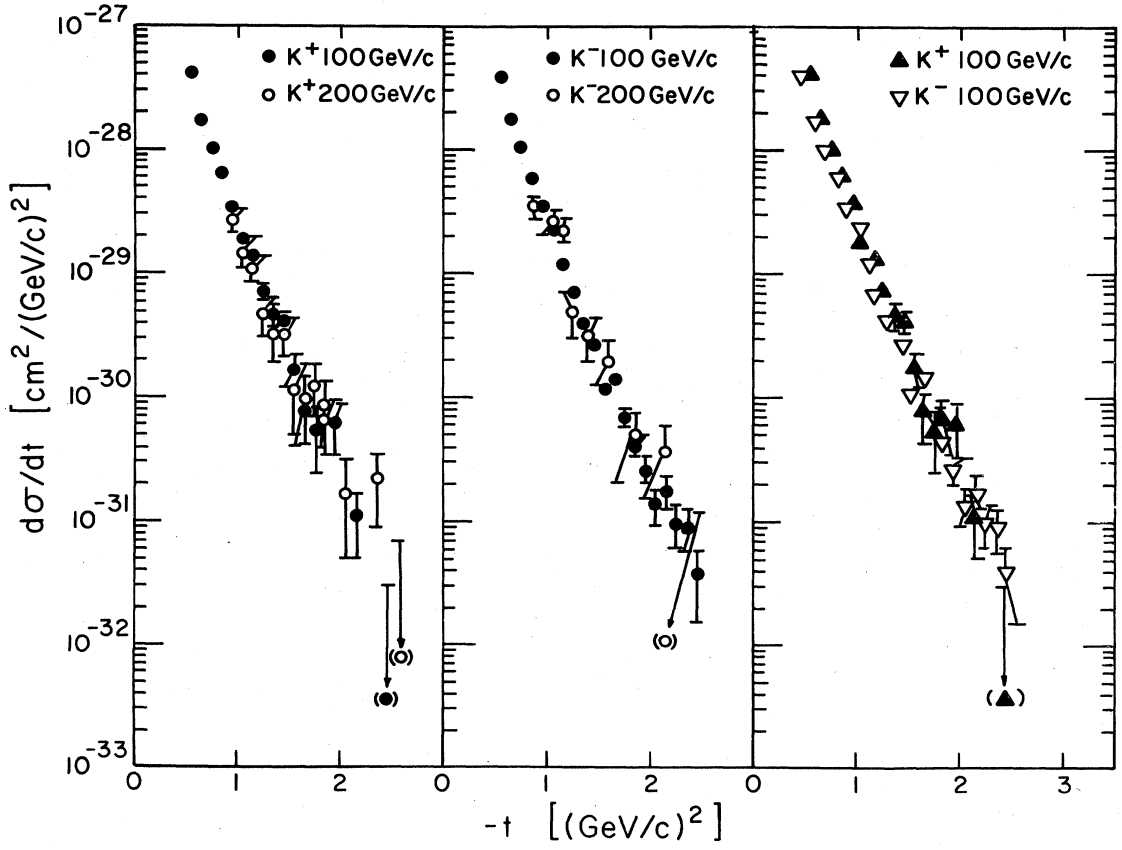

FIG. 20. $K^\pm p$ elastic scattering at 100 and 200 GeV/c.

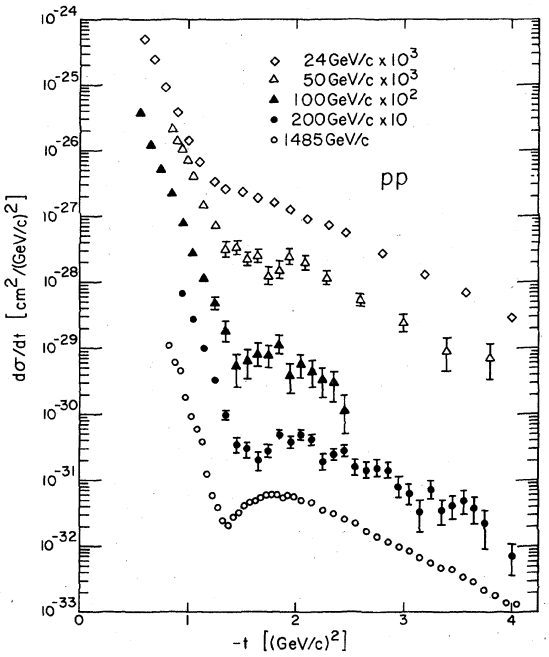

FIG. 21. Proton-proton elastic scattering between 24 and 1485 GeV/c. Data from this experiment and Refs. 14, 22, and 42.

same t value), indicating that a threshold momentum exists for this behavior as in the pp case; however, 50-GeV/c π^+p data[20] (Fig. 26) do show a small dip at about the same t value. Data on π^+p and π^-p below ~ 20 GeV/c both show a dip at $-t=2.8$ which dies away with

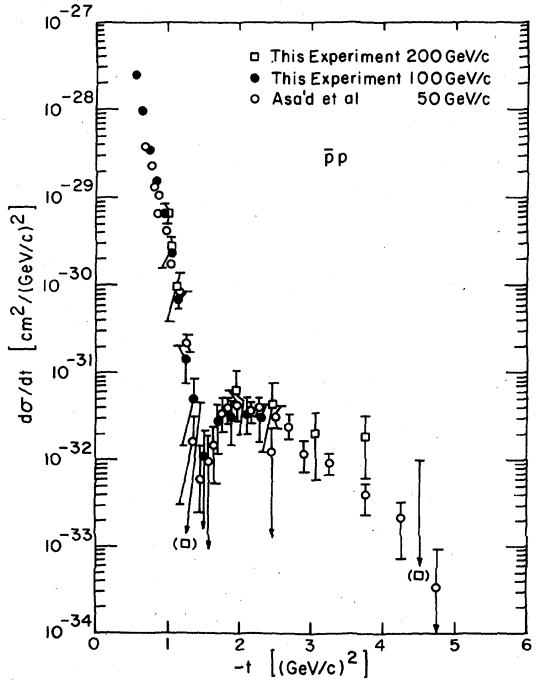

FIG. 22. Antiproton-proton elastic scattering at 100 and 200 GeV/c (this experiment) and 50 GeV/c (Ref. 19).

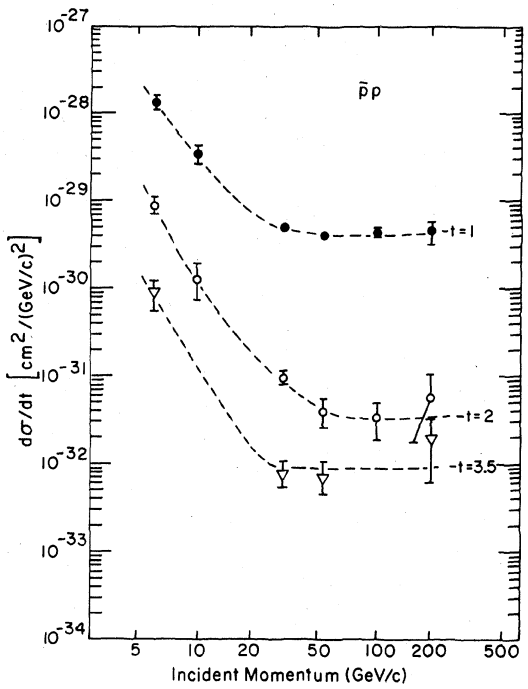

FIG. 23. Antiproton-proton elastic scattering. $d\sigma/dt$ at three values of $-t$ as a function of incident momentum. (Points are interpolated from data of this experiment and Refs. 19, 23, 45.) The curves are drawn to guide the eye.

increasing momentum; at 23 GeV/c it has become a small kink (Fig. 2), and at 50 GeV/c it has disappeared as seen in Figs. 25 and 26.

Apart from the dip region, there is little momentum

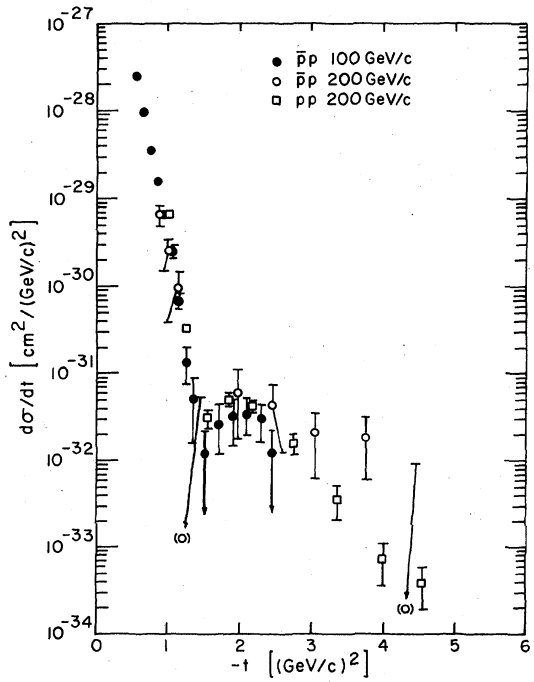

FIG. 24. Comparison of proton-proton and antiproton-proton elastic scattering. Not all points are plotted, for clarity.

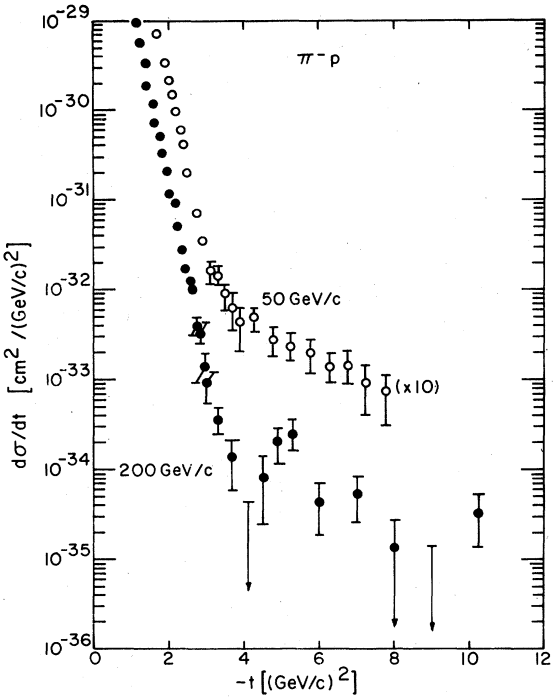

FIG. 25. $\pi^- p$ elastic scattering at 200 GeV/c (this experiment) and 50 GeV/c (Ref. 20).

dependence of the $\pi^- p$ cross section between 50 and 200 GeV/c. This is the expected behavior when the dominant scattering process is diffractive. Since the preliminary version of these results became available,[1] various models, which include diffraction, frequently of the Chou-Yang type, have been used to fit the data. (See, for example, Refs. 69–76.)

The pion form factor has been derived[72,73,77] from our 200-GeV/c $\pi^- p$ data using the Chou-Yang model.[25] As has been noted before,[27] the form factor obtained agrees well with the pion electromagnetic form factor obtained from pion electroproduction[28] where this information is available ($-t<2$), and the form factor slope near $t=0$ gives a value of the pion radius $r_\pi=0.66$ fm, in good agreement with that obtained from πe scattering.[29] As shown in Ref. 77, the form factor obtained from our data agrees with the vector-meson-dominance-model prediction for $-t \lesssim 1$, but there is significant disagreement at larger $-t$; however, there is reasonable agreement with a QCD prediction[32] which is expected to be valid in the large $-t$ region.

It would be of interest if the data at large $-t$ beyond the dip could be used to test the QCD predictions of Ref. 32. Unfortunately, there are no results at the same (or even close to the same) t/s but at different s, as was the case with large $-t$ pp scattering, so that no conclusions can be drawn.[43,44] In order to make a πp QCD test, 200-GeV/c measurements out to $-t \sim 20$ or 100 GeV/c measurements out to $-t \sim 10$ would be needed.

The QCD diagram proposed by Donnachie and Landshoff[33] predicts little s dependence, but a t dependence of the form $d\sigma/dt \propto |t|^{-7}$. In Fig. 27 there is a qualitative

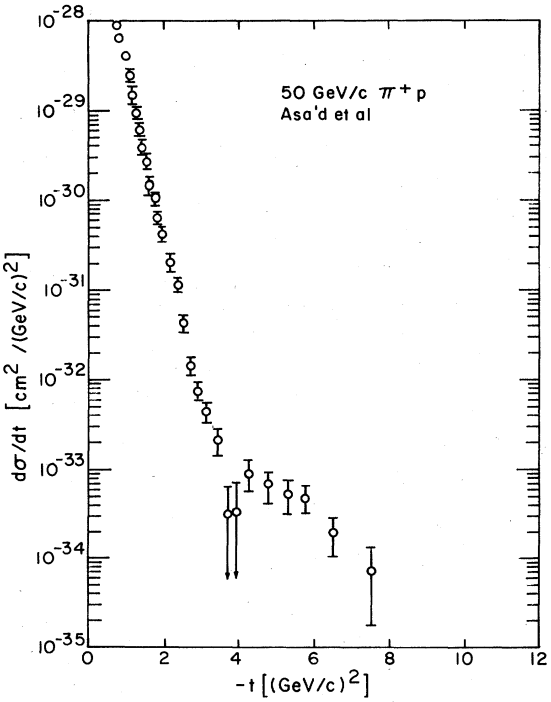

FIG. 26. $\pi^+ p$ elastic scattering at 50 GeV/c (figure from Ref. 20).

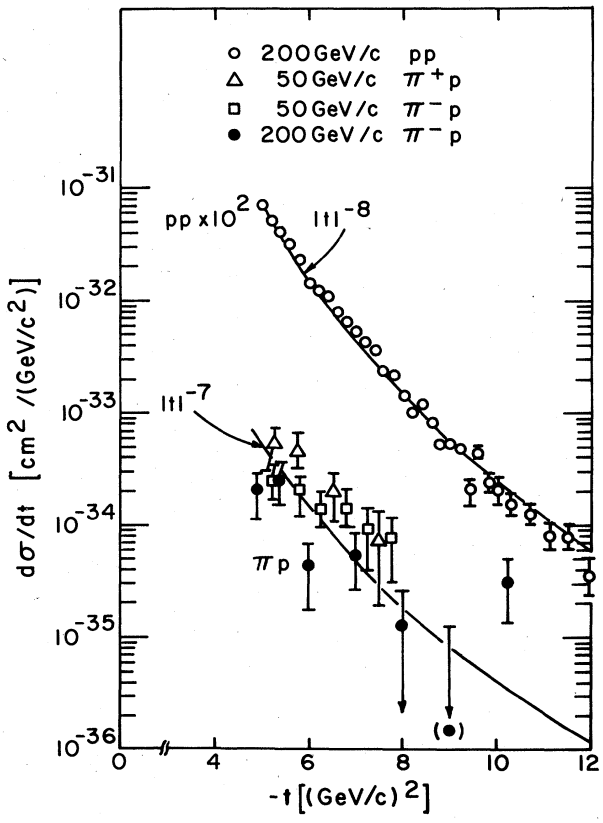

FIG. 27. Proton-proton elastic scattering data at 200 GeV/c (Ref. 13) compared to $|t|^{-8}$, together with πp data at 50 GeV/c (Ref. 20) and 200 GeV/c (this experiment) compared to $|t|^{-7}$.

suggestion of this behavior, but quantitatively the agreement is poor. A maximum-likelihood fit to our 200-GeV/c $\pi^- p$ results for $-t > 4.9$ of the form $d\sigma/dt \propto |t|^{-\alpha}$ gives $\alpha = 3.9 \pm 1.0$; for 50-GeV/c $\pi^- p$, $\alpha = 2.8 \pm 1.3$; and a combined fit gives $\alpha = 3.5 \pm 0.8$. In this figure we show also a corresponding pp fit, where good agreement of data and prediction is seen.

In pp scattering, the $|t|^{-8}$ behavior does not set in until $-t \gtrsim 4$, considerably beyond the diffraction dip position at $-t = 1.4$. One could speculate that quantitative agreement with the $|t|^{-7}$ behavior for πp will not set in until a t value at about the same factor above the dip, possibly at about $-t \sim 12$.

4. $\pi^{\pm} p$ and $K^{\pm} p$

Results for meson-proton cross sections are shown in Figs. 15–20. The $\pi^+ p$ data , shown in Fig. 19 together with 50 GeV/c results from Ref. 20, suggest a possible small dependence on incident momentum. Within the experimental uncertainties, there is no momentum or charge dependence of any of the other cross sections in the momentum and $-t$ range measured here. The data also show only small differences between kaon and pion cross sections in the range $1 \lesssim -t \lesssim 2.5$ at 100 and 200 GeV/c. Such approximate equality has been observed previously at 14 GeV/c over the same t range,[18] and at 50–200 GeV/c for $0.8 \lesssim -t \lesssim 1.5$.[10] 50-GeV/$c$ $K^+ p$ data[21] (see Fig. 28) show a small dip at $-t = 4$, somewhat similar to πp scattering.

Hadron-hadron elastic scattering has been used, via the Chou-Yang model, to obtain particle form factors as noted in the previous section. Results obtained in the past[27] for pions and kaons gave reasonable agreement with measured electromagnetic form factors[28] and radii;[29,30] little difference was observed between pion and kaon form factors, although the kaon radius obtained was slightly less than that of the pion. We have derived pion and kaon form factors out to $-t \sim 2.5$ using the data presented here, and also observe little difference between them.

The small difference between our K and π cross sections is illustrated in Fig. 29(a) by the 100-GeV/c data of this experiment for negative mesons together with lower $-t$ data[10] and the optical point (calculated using total cross section and real part of the forward-scattering amplitude data from Refs. 78–80). Although the π and K cross sections are always close in value, the K^- data fall more slowly with $-t$ than π^-; the two cross sections cross near $-t \sim 1$. These same features are observed at 200 GeV/c for negative mesons, and also for positive mesons at the same two momenta. In the past, differences

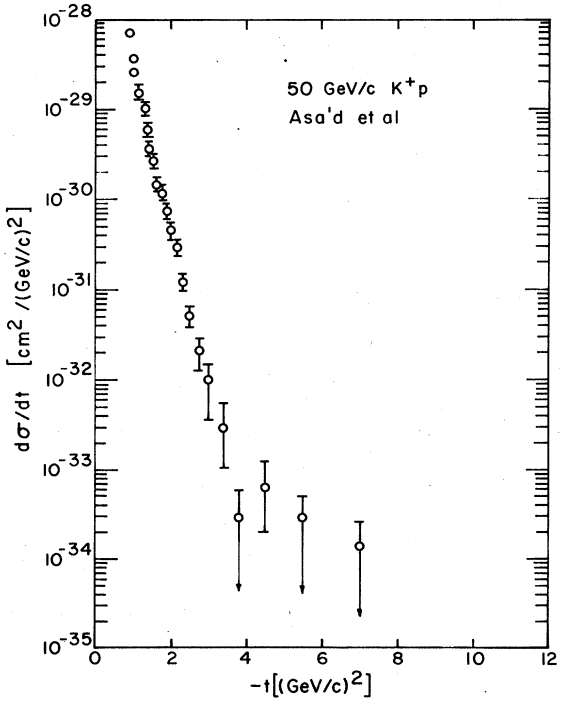

FIG. 28. $K^+ p$ elastic scattering at 50 GeV/c (figure from Ref. 21).

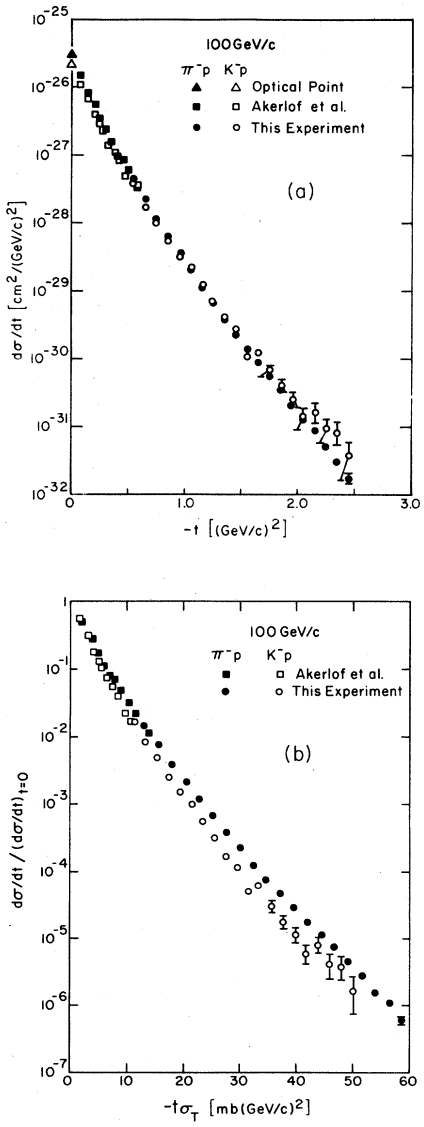

FIG. 29. Test of simple geometrical scaling at 100 GeV/c, using data from this experiment and Refs. 10, 78, 79, and 80.

between π and K data above 30 GeV/c have been explained[37,50] by a simple version of geometrical scaling. As discussed earlier, the π and K data become identical when $d\sigma/dt$ normalized to the optical point is plotted against $t\sigma_T$ for each incident particle (where σ_T is the particle-proton total cross section). We observe significant deviations from such simple geometrical-scaling behavior in our 100-GeV/c results, as illustrated in Fig. 29(b) for 100-GeV/c negative mesons; the statistical accuracy of these data, however, is higher than used in the previous comparisons. It should be noted that such deviations from simple geometrical scaling have been discussed before.[38,39] At 200 GeV/c, our results are in closer agreement with the simple geometrical scaling, but the statistical accuracy of the 200-GeV/c kaon data does not allow a definitive statement.

5. πp and pp

A comparison of 200-GeV/c $\pi^- p$ and pp elastic scattering is shown in Fig. 30. They are quantitatively different, although they do have many common features as discussed earlier. After a fall of many decades from the optical point, both show a diffraction dip (at $-t \sim 1.4$ for pp and $-t \sim 4$ for $\pi^- p$) followed by a second maximum and then a relatively slow fall with increasing $-t$.

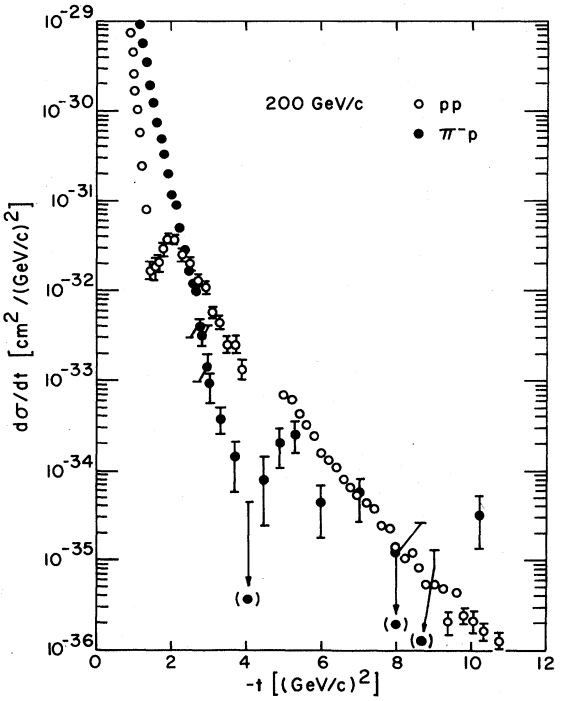

FIG. 30. Comparison of 200 GeV/c $\pi^- p$ and pp elastic scattering.

V. CONCLUSIONS

Results have been presented here on $\pi^{\pm} p$, $K^{\pm} p$, and $p^{\pm} p$ elastic scattering measured with an apparatus acceptance of $0.5 < -t < 2.5$ and $0.9 < -t < 11$ at 100 and 200 GeV/c, respectively. When taken together with other existing data, there is strong evidence that hadron-hadron elastic scattering above ~ 50 GeV/c is diffractive in the medium $-t$ region. There is little variation of any of the cross sections with incident momentum, and almost all of the processes now show a diffractionlike dip: for pp, $\bar{p}p$, and np, this dip is at $-t \sim 1.4$; for $\pi^- p$, $\pi^+ p$, and possibly $K^+ p$, the dip is at $-t \sim 4$. In addition, little difference is seen among the various meson-proton t distributions, and among the various baryon-proton t distributions.

At large $-t$, pp elastic-scattering results agree with the predictions of QCD; however, for πp, more data is needed in order to compare results at the same t/s but different s. A measurement of πp elastic scattering to $-t \sim 20$ at 100 and 200 GeV/c will help to test the large $-t$ QCD predictions. Data for $\bar{p}p$ out to $-t \sim 2$ or greater at the CERN and Fermilab colliders will enable tests of the diffractive nature of the small $-t$ scattering to be carried out.

ACKNOWLEDGMENTS

We wish to thank Hoshang Vaid and Carl Lindenmeyer for technical aid, the Fermilab Meson Department (especially Paul Czarapata, Herman Haggerty, Ernie Malamud, and Skip McGuire) for much assistance before and during the run, and Al Silverman for the loan of equipment. This work was supported by the U. S. Department of Energy and the National Science Foundation.

*Present address: Fairchild Republic, Farmingdale, NY 11735.
†Deceased.
‡Present address: Physics Department, Rutgers University, New Brunswick, NJ 08903.
§Present address: Physics Department, University of California at Santa Barbara, Santa Barbara, CA 93106.
**Present address: Physics Department, Colgate University, Hamilton, NY 13346.

[1]W. F. Baker *et al.*, Phys. Rev. Lett. **47**, 1683 (1981).
[2]D. H. Kaplan *et al.*, Phys. Rev. D **26**, 723 (1982).
[3]R. M. Kalbach *et al.*, Phys. Rev. D **27**, 2752 (1983).
[4]P. E. Karchin, Ph.D. thesis, Cornell University, 1982.
[5]D. H. Kaplan, Ph.D. thesis, Cornell University, 1983.
[6]K. W. Krueger, Ph.D. thesis, University of Arizona, 1983.
[7]S. F. McHugh, Ph.D. thesis, University of California at San Diego, 1983.
[8]In this paper, the units for $-t$ are (GeV/c^2).
[9]R. Rusak *et al.*, Phys. Rev. Lett. **41**, 1632 (1978).
[10]C. Akerlof *et al.*, Phys. Rev. D **14**, 33 2864 (1976).
[11]G. Fidecaro *et al.*, Nucl. Phys. **B173**, 513 (1980).
[12]G. Fidecaro *et al.*, Phys. Lett. **105B**, 309 (1981).
[13]W. Faissler *et al.*, Phys. Rev. D **23**, 33 (1981).
[14]E. Nagy *et al.*, Nucl. Phys. **B150**, 221 (1979).
[15]C. E. DeHaven *et al.*, Nucl. Phys. **B148**, 1 (1979).

[16]D. S. Ayres *et al.*, Phys. Rev. D **15**, 3105 (1977).
[17]A. Schiz *et al.*, Phys. Rev. D **24**, 26 (1981).
[18]R. Rubinstein *et al.*, Phys. Rev. Lett. **30**, 1010 (1973).
[19]Z. Asa'd *et al.*, Phys. Lett. **108B**, 51 (1982).
[20]Z. Asa'd *et al.*, Phys. Lett. **118B**, 442 (1982).
[21]Z. Asa'd *et al.*, Phys. Lett. **123B**, 265 (1983).
[22]Z. Asa'd *et al.*, Phys. Lett. **128B**, 124 (1983).
[23]Z. Asa'd *et al.*, Phys. Lett. **130B**, 335 (1983).
[24]C. Baglin *et al.*, Nucl. Phys. **B216**, 1 (1983).
[25]T. T. Chou and C. N. Yang, Phys. Rev. **170**, 1591 (1968).
[26]M. Kac, Nucl. Phys. **B62**, 402 (1973).
[27]D. S. Ayres *et al.*, Phys. Rev. D **14**, 3092 (1976).
[28]C. J. Bebek *et al.*, Phys. Rev. D **13**, 25 (1976); **17**, 1693 (1978).
[29]E. B. Dally *et al.*, Phys. Rev. Lett. **48**, 375 (1982).
[30]E. B. Dally *et al.*, Phys. Rev. Lett. **45**, 232 (1980).
[31]S. C. Chan *et al.*, Phys. Rev. D **17**, 802 (1978).
[32]P. Lepage and S. Brodsky, Phys. Rev. D **22**, 2157 (1980).
[33]A. Donnachie and P. V. Landshoff, Z. Phys. C **2**, 55 (1979).
[34]A. H. Mueller, Phys. Rep. **73**, 237 (1981).
[35]J. Dias de Deus, Nucl. Phys. **B59**, 231 (1973).
[36]A. J. Buras and J. Dias de Deus, Nucl. Phys. **B71**, 481 (1974).
[37]V. Barger, J. Luthe, and R. J. N. Phillips, Nucl. Phys. **B88**, 237 (1975).
[38]V. Barger and R. J. N. Phillips, Phys. Lett. **60B**, 358 (1976).
[39]J. Dias de Deus and P. Kroll, Phys. Lett. **60B**, 375 (1976); Nuovo Cimento **37A**, 67 (1977).
[40]G. Cocconi *et al.*, Phys. Rev. **138**, B165 (1965).
[41]C. Ankenbrandt *et al.*, Phys. Rev. **170**, 1223 (1968).
[42]J. V. Allaby *et al.*, Nucl. Phys. **B52**, 316 (1973).
[43]J. Orear, in *Proceedings of the XVIIth Rencontre de Moriond, Les Arcs, France, 1982,* edited by J. Tran Thanh Van (Editions Frontières, Gif-sur-Yvette, 1982), p. 359.
[44]R. Rubinstein, Bull. Am. Phys. Soc. **28**, 665 (1983); Fermilab Report No. FERMILAB-Conf-83/50-EXP, 1983 (unpublished).
[45]D. P. Owen *et al.*, Phys. Rev. **181**, 1794 (1969).
[46]D. Birnbaum *et al.*, Phys. Rev. Lett. **23**, 663 (1969).
[47]T. Buran *et al.*, Nucl. Phys. **B97**, 11 (1975).
[48]A. Berglund *et al.*, Nucl. Phys. **B176**, 346 (1980).
[49]P. Cornillon *et al.* Phys. Rev. Lett. **30**, 403 (1973).
[50]C. Bruneton *et al.*, Nucl. Phys. **B124**, 391 (1977).
[51]C. Baglin *et al.*, Nucl. Phys. **B98**, 365 (1975).
[52]C. Lewin *et al.*, Z. Phys. C **3**, 275 (1980).
[53]M. Y. Bogolyubskii *et al.*, Yad. Fiz. **33**, 126 (1981) [Sov. J. Nucl. Phys. **33**, 66 (1981)].
[54]M. Barth *et al.*, Z. Phys. C **16**, 111 (1982).
[55]J. R. Orr and A. L. Read, Meson Laboratory preliminary design report, Fermilab, 1971 (unpublished).
[56]E. Malamud, Fermilab Meson Department internal report, 1977 (unpublished).
[57]M. Benot, *et al.*, Nucl. Instrum. Methods **105**, 431 (1972).
[58]W. F. Baker, *et al.*, Phys. Rev. D **27**, 1999 (1983).
[59]H. Cunitz *et al.*, Nucl. Instrum. Methods **91**, 211 (1971).
[60]R. Galik, Ph.D. thesis, Cornell University, 1977.
[61]A. Browman, Cornell University LNS Memo No. TOP-6006-14 (unpublished).
[62]M. R. Sogard, Phys. Rev. D **9**, 1486 (1974).
[63]J. S. Klinger, Fermilab Report No. Fermilab-PUB-80/26-EXP, 1980 (unpublished).
[64]T. T. Chou and C. N. Yang, Phys. Rev. Lett. **46**, 764 (1982).
[65]J. P. Guillaud and M. M. Islam, University of Connecticut Report No. 80-0861, 1980 (unpublished).
[66]M. Bozzo *et al.*, Contribution to International Conference on High Energy Physics, Brighton, 1983 (unpublished).
[67]A. Donnachie and P. V. Landshoff, Phys. Lett. **123B**, 345 (1983).
[68]M. M. Islam, T. Fearnley, and J. P. Guillaud, CERN Report No. CERN-EP/83-96, 1983 (unpublished).
[69]S. V. Goloskokov *et al.*, JINR Dubna Report No. E2-82-109, 1982 (unpublished).
[70]Fazal-e-Aleem, Punjab University, report, 1982 (unpublished).
[71]S. Drenska *et al.*, JINR Dubna Report No. D2-82-280, 1982 (unpublished).
[72]C. H. Lai *et al.*, Phys. Lett. **122B**, 177 (1983); Phys. Rev. D **27**, 2214 (1983).
[73]C. Bourrely *et al.*, Phys. Lett. **132B**, 191 (1983).
[74]M. Hutt and I. S. Stefanescu, Karlsruhe University Report No. TKP 82-12, 1982 (unpublished).
[75]P. D. B. Collins and P. J. Kearney, Z. Phys. C **22**, 277 (1984).
[76]S. Sanielevici and P. Valin, Phys. Rev. D **29**, 52 (1984).
[77]P. Karchin and J. Orear, Cornell University Report No. CLNS-82/543, 1982 (unpublished).
[78]A. S. Carroll *et al.*, Phys. Lett. **61B**, 303 (1976); **80B**, 423 (1979).
[79]J. P. Burq *et al.*, Phys. Lett. **77B**, 438 (1978); **109B**, 111 (1982).
[80]L. A. Fajardo, *et al.*, Phys. Rev. D **24**, 46 (1981).